V899 MON: AN OUTBURSTING PROTOSTAR WITH A PECULIAR LIGHT CURVE, AND ITS TRANSITION PHASES

J. P. Ninan[1], D. K. Ojha[1], T. Baug[1], B. C. Bhatt[2], V. Mohan[3], S. K. Ghosh[4], A. Men'shchikov[5], G. C. Anupama[2], M. Tamura[6], and Th. Henning[7]

[1] Department of Astronomy and Astrophysics, Tata Institute of Fundamental Research, Homi Bhabha Road, Colaba, Mumbai 400 005, India; ninan@tifr.res.in
[2] Indian Institute of Astrophysics, Korama ngala, Bangalore 560 034, India
[3] Inter-University Centre for Astronomy and Astrophysics, Pune 411 007, India
[4] National Centre for Radio Astrophysics, Tata Institute of Fundamental Research, Pune 411 007, India
[5] Laboratoire AIM, CEA/DSM-CNRS-Université Paris Diderot, IRFU/SAp, CEA Saclay, Orme des Merisiers, F-91191 Gif-sur-Yvette, France
[6] National Astronomical Observatory of Japan, Mitaka, Tokyo 181-8588, Japan
[7] Max-Planck-Institute for Astronomy, Königstuhl 17, D-69117 Heidelberg, Germany

ABSTRACT

We present a detailed study of V899 Mon (a new member in the FUors/EXors family of young low-mass stars undergoing outburst), based on our long-term monitoring of the source starting from 2009 November to 2015 April. Our optical and near-infrared photometric and spectroscopic monitoring recorded the source transitioning from its first outburst to a short-duration quiescence phase (<1 yr), and then returning to a second outburst. We report here the evolution of the outflows from the inner region of the disk as the accretion rate evolved in various epochs. Our high-resolution ($R \sim 37,000$) optical spectrum could resolve interesting clumpy structures in the outflow traced by various lines. Change in far-infrared flux was also detected between two outburst epochs. Based on our observations, we constrained various stellar and envelope parameters of V899 Mon, as well as the kinematics of its accretion and outflow. The photometric and spectroscopic properties of this source fall between classical FUors and EXors. Our investigation of V899 Mon hints at instability associated with magnetospheric accretion being the physical cause of the sudden short-duration pause of the outburst in 2011. It is also a good candidate to explain similar short-duration pauses in outbursts of some other FUors/EXors sources.

Key words: protoplanetary disks – stars: early-type – stars: formation – stars: individual (V899 Mon) – stars: variables: T Tauri, Herbig Ae/Be – stars: winds, outflows

Supporting material: machine-readable tables

1. INTRODUCTION

Over the past few decades it has become increasingly evident that the process by which low-mass stars accrete gas from disks is an episodic process. A short-duration increase in accretion rate capable enough to deliver a substantial fraction of the final stellar mass has been observed in young sources over a wide spectrum of age from Class 0 to Class III (Safron et al. 2015). Traditionally, on the basis of the light curve and spectrum, these accretion outbursts are classified as FUors (showing decades-long outbursts with 4–5 mag change in optical and an absorption-line spectrum) and EXors (showing outbursts of a few months to years long with 2–3 mag change in optical and an emission-line spectrum) (Herbig 1977; Hartmann & Kenyon 1996; Hartmann 1998). These episodic outbursts can possibly solve some of the open issues in star formation like the "luminosity problem" (Kenyon et al. 1990; Evans et al. 2009) and the origin of knots in the outflows/jets from young stellar objects (YSOs; Ioannidis & Froebrich 2012). Recent discovery of these outbursts resulting in silicate crystallization in EX Lup shows the importance of this phenomenon in planet and comet formation (Ábrahám et al. 2009). Episodic accretion can also significantly change the pre-main-sequence isochrones used extensively for initial mass function studies and age/mass estimation of YSOs (Baraffe et al. 2012). From the number statistics it is estimated that every low-mass star undergoes ~50 such short-duration outbursts during its formation stage (Scholz et al. 2013). But the short duration of outbursts (months/years) with respect to

the million-year timescale of formation makes these events extremely rare to detect in star-forming regions. Various models based on instabilities have been proposed to explain this episodic nature of accretion, but so far every newly discovered FUors/EXors poses a new challenge for the models to explain the observed light curves.

We report here our long-term monitoring of the very peculiar outburst source V899 Monoceros, which gives significant insight into the mechanism of triggering and quenching of this class of outbursts. A possible FUor-type eruption of V899 Mon (aka IRAS 06068–0641) located near the Monoceros R2 region ($d \sim 905$ pc; Lombardi et al. 2011) was first discovered by the Catalina Real-time Transient Survey (CRTS) and reported by Wils et al. (2009). They announced the source as a FUor candidate based on the constant brightening it has been undergoing since 2005. The spectrum published by Wils et al. (2009) showed strong Hα and Ca II IR triplet lines, which identify the outbursting source as a YSO.

We started our long-term multiwavelength observations of this source in 2009 and could track the source undergoing transition from the first outburst phase to the quiescent phase, and finally returning to a second outburst within a year of quiescence. Our multiwavelength data provide a consistent picture on the physical processes that might have led to these sudden transitions in the accretion rate of V899 Mon.

In this paper we present the results of our long-term observations of V899 Mon. In Section 2 we describe observational details and data reduction procedures of photometric and spectroscopic data. In Section 3 we present our

Table 1
Observation Log of V899 Mon

Date	JD	FWHM[a]	Filter(s)/Grism(s)	Instrument(s)
2009 Nov 30	2,455,166	1″9	V, R, gr8	HFOSC
2009 Dec 04	2,455,170	3″1	V, R, I	HFOSC
2009 Dec 16	2,455,182	1″8	V, R, I	HFOSC
2009 Dec 17	2,455,183	…	gr7, gr8	HFOSC

Note.
[a] Measured average FWHM. This is a measure of the seeing.

(This table is available in its entirety in machine-readable form.)

results and deduction procedures. In Section 4 we discuss possible physical reasons for the short duration of the quiescence phase between the first and second outbursts. We conclude in Section 5 with major results we have obtained on V899 Mon, as well as its implications in understanding the general FUors/EXors outburst phenomenon.

2. OBSERVATIONS

2.1. Optical Photometry

Our long-term optical monitoring of V899 Mon started on 2009 November 30. The observations were carried out using the 2 m Himalayan Chandra Telescope (HCT) at the Indian Astronomical Observatory, Hanle (Ladakh), belonging to the Indian Institute of Astrophysics (IIA), India, and the 2 m telescope at the IUCAA (Inter-University Centre for Astronomy and Astrophysics) Girawali Observatory (IGO), Girawali (Pune), India. For optical photometry, the central $2K \times 2K$ CCD section of the Himalaya Faint Object Spectrograph and Camera (HFOSC) with a pixel scale of $0''296$ was used on the HCT, and the $2K \times 2K$ CCD of the IUCAA Faint Object Spectrograph & Camera (IFOSC) with a similar pixel scale of $0''3$ was used on the IGO. This gave us a field of view (FOV) of $\sim 10 \times 10$ arcmin^2 on both HCT and IGO. A detailed description of the instruments and telescopes is available at the IAO[8] and IGO[9] websites. V899 Mon's field ($(\alpha, \delta)_{2000} = 06^h09^m19^s28, -06°41'55''4$) was observed in standard $UBVRI$ Bessel filters. We carried out observations for 69 nights, out of which 41 nights were observed through HCT and the remaining ones from IGO. The photometric observation log is given in Table 1. Only a portion of the table is provided here. The complete table is available in machine-readable form in the online journal.

The standard photometric data reduction steps like bias subtraction, median flat-fielding, and finally aperture photometry of V899 Mon were done using our publicly released[10] pipeline for these instruments. Since V899 Mon source is quite bright and is not affected by any bright nebulosity, we used a $4 \times$ FWHM aperture for optical photometry. The background sky was estimated from a ring outside the aperture radius with a width of $4''5$. Magnitude calibration was done by solving color transformation equations for each night using Landolt's standard star field SA 98 (Landolt 1992) and the five field stars (see Figure 1) that we identified to have a stable magnitude over the period of our observations.
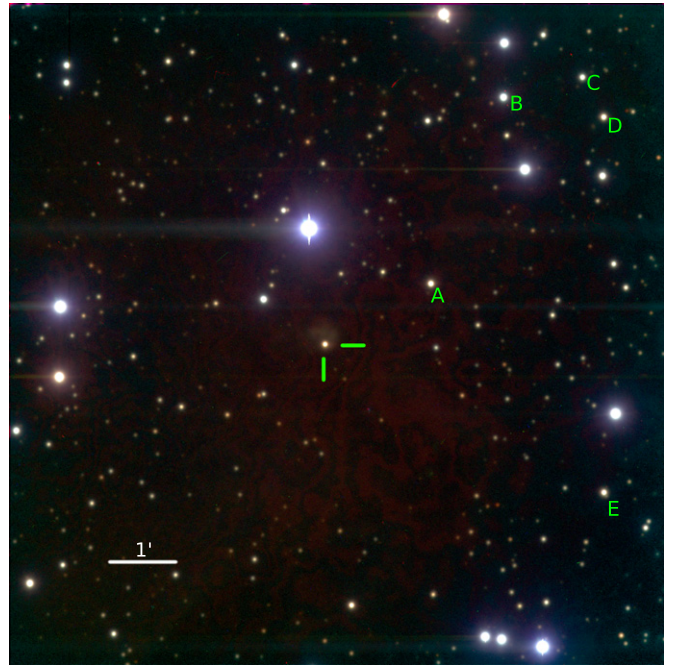
Figure 1. RGB color composite optical image of V899 Mon taken with HFOSC from HCT (V: blue; R: green; I: red) on 2011 January 2. V899 Mon was in its short-duration quiescent phase at this epoch. The FOV is $\sim 10 \times 10$ arcmin^2. North is up and east is to the left-hand side. Stars marked as A, B, C, D, and E are the secondary standard stars used for magnitude calibration. The location of V899 Mon is marked with two perpendicular lines at the middle.

2.2. NIR Photometry

Near-infrared (NIR) photometric monitoring of the source in J, H, and K/K_S bands was carried out using the HCT NIR camera (NIRCAM), the TIFR Near Infrared Spectrometer and Imager (TIRSPEC) mounted on HCT, and the TIFR Near Infrared Imaging Camera-II (TIRCAM2) mounted on the IGO telescope. NIRCAM has a 512×512 mercury cadmium telluride (HgCdTe) array, with a pixel size of $18 \mu m$, which gives an FOV of $\sim 3.6 \times 3.6$ arcmin^2 on HCT. Filters used for observations were J ($\lambda_{center} = 1.28 \mu m$, $\Delta\lambda = 0.28 \mu m$), H ($\lambda_{center} = 1.66 \mu m$, $\Delta\lambda = 0.33 \mu m$), and K ($\lambda_{center} = 2.22 \mu m$, $\Delta\lambda = 0.38 \mu m$). Further details of the instrument are available at http://www.iiap.res.in/iao/nir.html. TIRSPEC has a 1024×1024 Hawaii-1 PACE[11] (HgCdTe) array, with a pixel size of $18 \mu m$, which gives an FOV of $\sim 5 \times 5$ arcmin^2 on HCT. Filters used for observations were J ($\lambda_{center} = 1.25 \mu m$, $\Delta\lambda = 0.16 \mu m$), H ($\lambda_{center} = 1.635 \mu m$, $\Delta\lambda = 0.29 \mu m$), and K_S ($\lambda_{center} = 2.145 \mu m$, $\Delta\lambda = 0.31 \mu m$) (Mauna Kea Observatories near-infrared filter system). Further details of TIRSPEC are available in Ninan et al. (2014) and Ojha et al. (2012). TIRCAM2 has a 512×512 indium antimonide (InSb) array with a pixel size of $27 \mu m$. Filters used for observations were J ($\lambda_{center} = 1.20 \mu m$, $\Delta\lambda = 0.36 \mu m$), H ($\lambda_{center} = 1.66 \mu m$, $\Delta\lambda = 0.30 \mu m$), and K ($\lambda_{center} = 2.19 \mu m$, $\Delta\lambda = 0.40 \mu m$). More details on TIRCAM2 are available in Naik et al. (2012). The log of NIR observations is listed in Table 1. We have photometric observations for a total of 25 nights in the NIR. Our first JHK observation was carried out during the peak of the first outburst on 2010 February 20, and the remaining
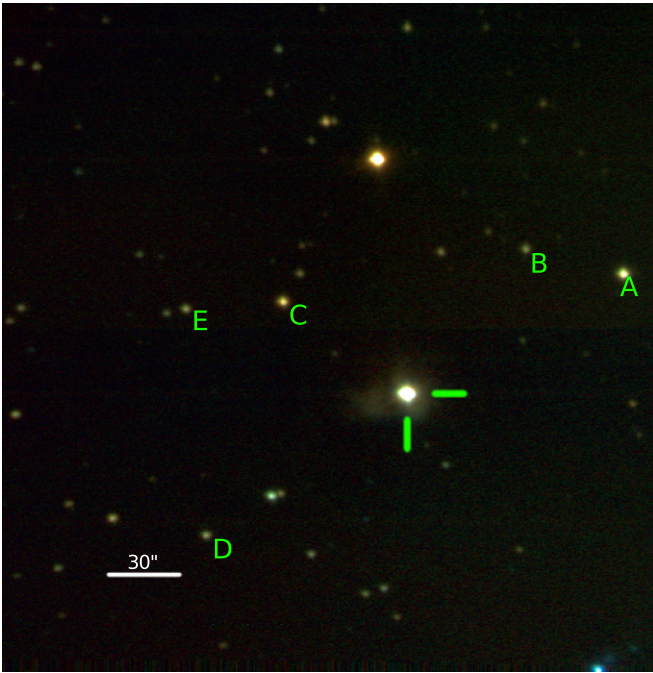
Figure 2. RGB color composite NIR image of V899 Mon taken with TIRSPEC from HCT (*J*: blue; *H*: green; K_S: red) on 2013 November 14. V899 Mon was in its second outburst phase at this epoch. The FOV is $\sim 5 \times 5$ arcmin^2. North is up and east is to the left-hand side. Stars marked as A, B, C, D, and E are the secondary standard stars used for magnitude calibration. The location of V899 Mon is marked with two perpendicular lines at the middle.

observations were carried out during the current ongoing second outburst.

NIR observations were carried out by the standard telescope dithering procedure. Five dither positions were observed. All the dithered object frames were median combined to generate master sky frames for NIRCAM and TIRCAM2. We combined twilight flats and all non-extended source frames observed during the same night to create accurate flats for each night. For NIRCAM and TIRCAM2, data reduction and final photometry were performed using the standard tasks in IRAF, while the TIRSPEC data were reduced using our TIRSPEC photometry pipeline (Ninan et al. 2014). For aperture photometry we used an aperture of $3 \times$ FWHM and the background sky was estimated from an annular ring outside the aperture radius with a width of 4″5. Magnitude calibration was done by solving color transformation equations for each night using Hunt's standard star fields AS 13 and AS 9 (Hunt et al. 1998) and the five field stars (labeled in Figure 2) that we identified to have a stable magnitude and that are consistent with 2MASS[12] over the period of our observations.

2.3. Medium-resolution Optical Spectroscopy

Our medium-resolution ($R \sim 1000$) optical spectroscopic monitoring of V899 Mon also started on 2009 November 30. The spectroscopic observations were carried out using both HCT and IGO. The full $2K \times 4K$ section of the HFOSC CCD spectrograph was used for HCT observations, and the $2K \times 2K$ IFOSC CCD spectrograph was used for IGO observations. These observations were done in the effective wavelength range of 3700–9000 Å, using grism 7 (center

wavelength 5300 Å) and grism 8 (center wavelength 7200 Å). The spectral resolution obtained for grism 7 and grism 8 with the 150 μm slit at IGO and the 167 μm slit at HCT was $\sim$7 Å. The log of spectroscopic observations is listed in Table 1. We have 8 spectra from the first outburst phase, 4 from the short quiescent phase, and 30 from the ongoing second outburst phase.

For wavelength calibration, we have used FeNe, FeAr, and HeCu lamps. Standard IRAF tasks like *APALL* and *APSUM* were used for spectral reduction using our publicly released PyRAF[13]-based pipeline developed for both the HFOSC and IFOSC instruments.

2.4. High-resolution Optical Spectroscopy

We acquired a high-resolution ($R \sim 37,000$) spectrum of V899 Mon during its second outburst phase on 2014 December 22 using the Southern African Large Telescope High Resolution Spectrograph (SALT-HRS) (Bramall et al. 2010). Both the red arm (5490–8810 Å) and the blue arm (3674–5490 Å) of the HRS instrument were used, to take a single exposure of 3170 s. For this medium-resolution instrument mode of HRS, it uses a 2″23 fiber to collect light from the target source, and another fiber of the same diameter is used to sample a nearby patch of the sky. Apart from target frames, the ThAr arc lamp spectrum was also taken through the sky fiber for wavelength calibration.

All the SALT-HRS data reduction was done by writing a reduction tool in Python, making use of *scikit-image* (van der Walt et al. 2014), *scipy* (Jones et al. 2001), *numpy* (van der Walt et al. 2011), and *astropy* (Astropy Collaboration et al. 2013). The additive factor to translate observed velocities in the spectrum to heliocentric velocities was found to be +0.92 km s^{-1} using the *rvcorrect* task in IRAF.

2.5. NIR Spectroscopy

NIR (1.02–2.35 μm) spectroscopic monitoring of V899 Mon started on 2013 September 25 using TIRSPEC mounted on HCT. Depending on the seeing conditions, slits with 1″48 or 1″97 widths were used. Spectra were taken in at least two dithered positions inside the slit. Spectra of an argon lamp for wavelength calibration and a tungsten lamp for the continuum flat were also taken immediately after each observation without moving any of the filter wheels. For telluric line correction, bright NIR spectroscopic standard stars within a few degrees and similar airmasses were observed immediately after observing the source. The typical spectral resolution obtained in our spectra is $R \sim 1200$. The log of spectroscopic observations is listed in Table 1. It may be noted that all 12 NIR spectral observations are taken during the current ongoing second outburst phase.

NIR spectral data were reduced using the TIRSPEC pipeline (Ninan et al. 2014). After wavelength calibration, the spectrum of V899 Mon was divided by a standard star spectrum to remove telluric lines and detector fringes seen in *H* and *K* orders' spectra. This continuum-corrected spectrum was scaled using the flux estimated from photometry to obtain the flux-calibrated spectrum. Since we do not have *Y*-band photometry, we interpolated *I*-band and *J*-band λf_λ flux to *Y* band and used the interpolated flux to scale the *Y*-band spectrum flux.

---

[12] Two Micron All Sky Survey.

[13] PyRAF is a product of the Space Telescope Science Institute, which is operated by AURA for NASA.

2.6. GMRT Radio Continuum Imaging

Continuum interferometric observation of V899 Mon at 1280 MHz with 33.3 MHz bandwidth was carried out on 2014 October 17 using the Giant Metrewave Radio Telescope (GMRT), Pune, India. GMRT consists of 30 dish antennas (each 45 m in diameter) in hybrid "Y" configuration (Swarup et al. 1991). Out of these, 25 antennas were online during our observation. The standard flux calibrator 3C 147 was observed for 15 minutes at the beginning and end of the observations. For phase calibration, the nearby Very Large Array calibrator 0607-085 was observed for 10 minutes after every 20 minutes of integration on V899 Mon. The total integration on the V899 Mon source was 4.5 hr.

CASAPY software was used for the data reduction. After careful iterative bad data flagging and gain calibration, we imaged the large FOV of $28' \times 28'$ by dividing the field into 128 w-projection planes using the *CLEAN* algorithm.

2.7. Herschel Far-infrared Photometry

We obtained imaging observations of the V899 Mon region in SPIRE[14] 250, 350, and 500 μm and PACS[15] 70 and 160 μm from the *Herschel* data archive.[16] SPIRE data were available for two epochs, one on 2010 September 4 (Proposal ID: KPGT_fmotte_1) and another on 2013 March 16 (Proposal ID: OT1_rgutermu_1). PACS data of V899 Mon were only available in the later epoch. Data from both the epochs were reduced using the standard *Herschel*'s HIPE pipeline with the latest calibration file. For point-source aperture photometry of V899 Mon we first tried the *sourceExtractorSussextractor* routine in HIPE on level 2 SPIRE data and the *multiplePointSourceAperturePhotometry* routine on PACS data. We also tried point-spread function (PSF) photometry using the *daophot* tool in IRAF. Since all these algorithms use an annular ring for background estimation and the background is highly nonuniform, the results were found to be very sensitive to aperture and background estimates. We finally estimated fluxes using *getsources* (Men'shchikov et al. 2012), which uses a linearly interpolated background estimate. These estimates were found to be consistent with the differential flux between two epochs (differential flux could be estimated more accurately since the subtracted image has a uniform background). The HIPE pipeline assumes a spectral energy distribution (SED) color, $\alpha = -1$ (where $F_{\nu} = \nu^{\alpha}$). The actual color α of V899 Mon was obtained from our flux estimates, and the corresponding color correction factor was multiplied to the flux values for obtaining color-corrected flux estimates.

2.8. WISE Photometry

We obtained imaging observations of the V899 Mon region in *W1* (3.4 μm), *W2* (4.6 μm), *W3* (12 μm), and *W4* (22 μm) bands from the *Wide-field Infrared Survey Explorer* (*WISE*) data archive (Wright et al. 2010). Photometric magnitude estimates were also available in the *WISE* all-sky catalog. *W1* and *W2* bands were observed at two epochs in 2010 March 17 and September 24, whereas *W3* and *W4* were observed only on 2010 March 17. Since *W1* and *W2* intensity maps looked

severely saturated, we have used only *W3* and *W4 WISE* catalog magnitudes for our study.

In this paper, we have also compiled all other publicly available archival data of this region at different epochs. Data were obtained from the following surveys and instruments: CRTS DR2,[17] POSS survey,[18] USNO-B catalog,[19] *IRAS* survey,[20] DENIS survey,[21] 2MASS,[22] AKARI,[23] IRAC,[24] and MIPS.[25]

3. RESULTS AND ANALYSIS

3.1. Photometric Results: Light Curves and Color Variations

An extended fan-shaped optical reflection nebula is typically seen around FUors. In the case of V899 Mon we detect only a small, faint, fan-shaped reflection nebula toward the north (see Figure 1). *U*, *B*, *V*, *R*, *I*, *J*, *H*, and K_S magnitudes of V899 Mon from our long-term continuous monitoring are listed in Table 2. Typical magnitude errors are less than 0.03 mag. Only a portion of the table is provided here. The complete table is available in machine-readable form in the online journal. The *R*-band magnitude light curve is shown in Figure 3. Effective *R*-band magnitudes[26] from CRTS are overplotted in the same graph for displaying the complete picture of the initial rise of the first outburst. Images of the V899 Mon field observed on 1953 December 29, 1983 December 29, 1989 January 9, and 2000 February 8 are available from digitized POSS-1 and POSS-2 archives. Magnitudes at the two epochs (1953 and 1989) that used the *R*-band filter are also shown in Figure 3. It should be noted that even though these magnitudes available in the USNO-B1.0 catalog are corrected for the non-standard bandpass filter used in the POSS-I survey, their variation seen between 1953 and 1989 might still be due to systematics in calibration. Few other outburst sources like V1647 Ori, V582 Aur, and V2492 Cyg have also shown such a sudden brief transition to quiescent phase after reaching the peak of the first outburst (Kóspál et al. 2013; Ninan et al. 2013; Semkov et al.

Table 2
Magnitudes of V899 Mon

JD	U	B	V	R	I	J	H	K_S
2,455,166	…	…	14.57	13.40	…	…	…	…
2,455,170	…	…	14.22	13.10	12.08	…	…	…
2,455,182	…	…	13.61	12.65	11.57	…	…	…
2,455,186	…	…	13.51	12.37	11.37	…	…	…

Note. Errors on *U*, *B*, *V*,*R*, and *I* magnitudes are <0.02 mag, TIRSPEC *J*, *H*, and K_S magnitudes have errors <0.02 mag, and TIRCAM2 and NIRCAM *J*, *H*, and *K* magnitudes have errors <0.06 mag.

(This table is available in its entirety in machine-readable form.)

---

[14] Spectral and Photometric Imaging Receiver.
[15] Photoconductor Array Camera and Spectrometer.
[16] *Herschel* is an ESA space observatory with science instruments provided by European-led Principal Investigator consortia and with important participation from NASA.

---

[17] Catalina Real-time Transient Survey Data Release 2.
[18] Palomar Observatory Sky Survey.
[19] U.S. Naval Observatory B1.0 Catalog.
[20] *Infrared Astronomical Satellite*, Survey.
[21] Deep Near Infrared Survey of the Southern Sky.
[22] Two Micron All Sky Survey.
[23] Akari All-Sky Survey Point Source Catalog.
[24] Infrared Array Camera on *Spitzer*.
[25] Multi-band Imaging Photometer on *Spitzer*.
[26] CRTS DR2 $V_{\rm CSS}$ magnitudes of V899 Mon were converted to effective R magnitude using color correction equation $V = V_{\rm CSS} + 0.91*(V - R)^2 + 0.04$ and $V - R = 1.11$. http://nesssi.cacr.caltech.edu/DataRelease/FAQ2.html#improve.
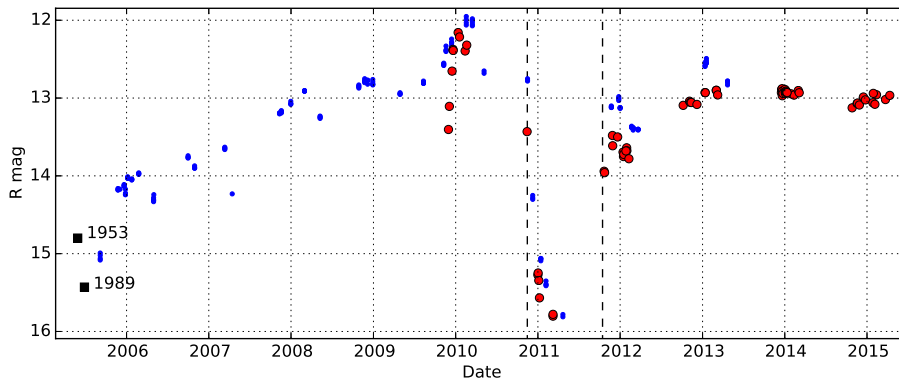
Figure 3. Light curve of V899 Mon showing its first outburst, short quiescent phase, and current ongoing second outburst phase. Red circles are R-band magnitudes from our observations, and blue circles are CRTS magnitudes converted to R magnitudes. POSS-1 and POSS-2 epochs' R magnitudes are also shown for comparison as black squares.

2013). V582 Aur and V2492 Cyg's light curves were very unstable, but V1647 Ori's light curve was very similar to V899 Mon in terms of the stability during the phase transitions.

One possible scenario that could explain the sudden dimming of the source in 2011 is occultation by a dust clump. By taking the dust size parameter R_V and change in extinction A_V as free parameters, we tried to fit the observed change in magnitudes of V, R, I, J, H, and K_S bands[27] between the first outburst and quiescent phases (i.e., 2.86, 2.90, 3.06, 2.96, 2.75, and 2.36 Δ mag, respectively, in each band). Coefficients in Table 2 of Cardelli et al. (1989) were used for calculation, and no positive value of R_V could fit the observed changes in magnitudes. Hence, we can safely conclude that the quiescent phase in 2011 was due to an actual break in the outburst and is not due to dust occultation. Even though we have not considered scattered excess blue light (like in UX Ori systems) in the above analysis, an almost similar magnitude drop ($\sim$2.8) in optical and NIR magnitudes to the pre-outburst phase makes it unlikely to be a case of dust obscuration. A stronger argument against the dust obscuration scenario comes from the observed variation in spectral line fluxes during this transition (see Section 3.4). The relative flux changes observed in various spectral lines cannot be explained by a simple change in extinction.

Figure 4 shows the NIR $J - H/H - K$ color–color (CC) diagram. The position of V899 Mon in it shows no significant extinction to the source, and it falls on the classical T Tauri (CTT) locus. The positions in the CC diagram during first and second outbursts are also different from each other. But since we have only one NIR observation from the rapidly varying ending phase of the first outburst, it might not be a good representation of the NIR color of the first outburst. The green squares measured during the 2013–2015 period of the second outburst show small movements along the reddening vector. Such short-period, small-amplitude fluctuations during the outburst phase are also seen in other FUor/EXor objects (Ninan et al. 2013; Semkov et al. 2013; Audard et al. 2014). Unlike the quiescence in 2011, these short variations in the second outburst could be due to small dust clump occultations or minor fluctuations in the accretion. The NIR $J/J - K$ color–
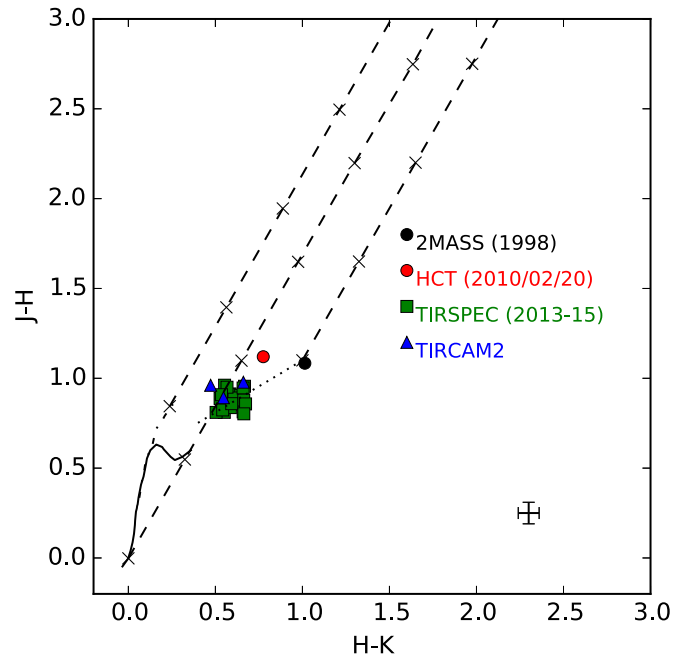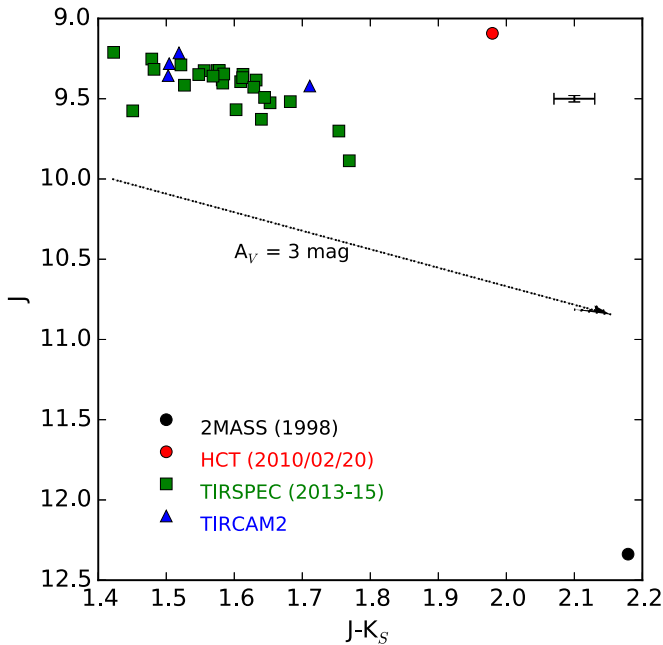

Figure 4. Positions of V899 Mon in the $J - H/H - K$ CC diagram during the quiescent phase (black circle), first outburst phase (red circle), and second outburst phase (green squares and blue triangles). The solid curve shows the locus of field dwarfs, and the dot-dashed curve shows the locus of giants (Bessell & Brett 1988). The dotted line represents the locus of classical T Tauri (CTT) stars (Meyer et al. 1997). The diagonal straight dashed lines show the reddening vectors (Rieke & Lebofsky 1985), with crosses denoting an A_V difference of 5 mag. Typical error bars of each data point are shown in the bottom right corner.

magnitude diagram (CMD) (see Figure 5) also indicates the general trend of V899 Mon getting redder (bluer) when it dims (brightens).

3.1.1. Outburst—Quiescent Transition Phase

In contrast to existing FUor/EXor observations in the literature, we could carry out several observations of V899 Mon during its transition from outburst phase to quiescent phase and back. Figure 6 shows the V-band magnitude light curve of the source, color-coded with $V - R$ color in the outer ring and $V - I$ color at the center. These colors indicate that the object was reddest during the transition stages rather than during the outburst or quiescent phases. It could imply that the

---

[27] Even though we do not have NIR photometric measurements during quiescent phase in 2011, our quiescent phase I-band magnitude matches with the DENIS I magnitude observed on 1999 January 25, and DENIS J and K magnitudes of this epoch match with 2MASS J and K_S magnitudes observed in 1998. Hence, in this study we have taken 2MASS magnitudes as the quiescent phase J, H, and K_S magnitudes of the V899 Mon source.

Figure 5. NIR $J/J-K$ color–magnitude diagram showing the movement of V899 Mon during its quiescent phase (black circle), first outburst phase (red circle), and second outburst phase (green squares and blue triangles). The arrow shows the reddening vector (Rieke & Lebofsky 1985), which corresponds to an A_V of 3 mag. Typical error bars of each data point are shown in the top right corner.

extra flux component of the outburst was cooler at the beginning and became hotter as the outburst reached its peak. Since the transition phase flux was cooler than the quiescent phase, outburst flux could not have initially originated on the surface of the hot central star; rather, it might have originated in the disk. This is the first direct observational evidence to support triggering of outbursts in the disk of FUors/EXors. The color change seen in this plot could be a combined effect of both change in extinction and change in temperature. Figure 7 shows the V-, R-, and I-band light curves color-coded with an extinction invariant quantity. The y-intercept along the reddening vector in any CC diagrams, for example, $C_{VRI} = (V-R) - (R-I)*E(V-R)/E(R-I)$ (McGehee et al. 2004), is a weighted difference of two colors, which is invariant to change in extinction A_V. While it is not possible to completely separate out the degenerate SED slope change due to temperature and extinction change, any change in this extinction invariant color implies real change in the intrinsic SED slope (temperature). V899 Mon shows significant change in C_{VRI} between the end of the first outburst phase, quiescent phase, transition stage, and ongoing second outburst phase. Significant variation is also seen during the peak of the first outburst, implying that the temperatures of the source during those epochs were different than the ongoing second outburst. However, since C_{VRI} is a weighted difference between two colors and could not tell unambiguously whether the intrinsic slope of the SED became red or blue, Figure 7 only indicates change in the intrinsic slope of the SED (temperature). It does not clarify whether reddening of flux during the transition stage was due to temperature change alone or was due to the combined effect of a short-term increase in extinction and change in temperature.

3.2. Stellar Properties

V899 Mon was observed in *WISE* 12 and 22 μm bands on 2010 March 17, within 1 month after our NIR observations in *J, H*, and *K* bands from HCT on 2010 February 20 (first outburst peak). We utilized them to estimate the conventional infrared logarithmic slope of the spectrum α (where $\lambda F_\lambda = \lambda^\alpha$) used for age classification of YSOs. During the peak outburst phase (2010 March), we obtained a slope $\alpha = -0.27$ between 2.16 and 11.56 μm and $\alpha = -0.51$ between 11.56 and 22 μm. These values classify V899 Mon as a flat-spectrum or an early Class II YSO (Greene et al. 1994) during its peak outburst phase.

$U-B$, $B-V$, $V-R$, and $R-I$ colors of Siess et al. (2000) isochrones can be used to constrain photometrically the mass, age, and extinction of the source. This is done by finding a region in the mass, age, and extinction parameter space in which colors predicted by the Siess et al. (2000) model are consistent with all the observed optical colors of V899 Mon. For this analysis we sampled Siess et al. (2000) isochrones in its valid age range 0.01–100 Myr and mass range 0.1–7 $M_\odot$ in log space. Nonuniform rectangular mass versus age grids were generated for each of the $U-B$, $B-V$, $V-R$, and $R-I$ colors by interpolating (using 2D Bi-spline) colors predicted by the Siess et al. (2000) isochrones. $U-B$ and $B-V$ colors of V899 Mon during the second outburst and $V-R$ and $R-I$ quiescent phase colors were used for fixing the position of V899 Mon in this four-dimensional color space. The errors of the color estimates were taken to be 0.1 mag, which correspond to a symmetric 4D Gaussian in color space. The radial basis function was used to calculate the distance to the source for each point in the mass–age grid. A contour was plotted for regions within 1σ distance from V899 Mon's position. These contours were repeatedly estimated for various values of A_V ranging from 0.5 to 8 mag (see Figure 8). As seen in the figure, $A_V < 2.2$ mag and $A_V > 4.0$ mag will make all Siess et al. (2000) isochrone colors incompatible with V899 Mon and hence can be ruled out. Owing to the correlation between age and mass, we obtain tight constraints only for A_V from this analysis. Even though the analysis was done for all possible age ranges, since V899 Mon is a heavy disk accreting source, we expect its position inside contours to be only around the region where age is $\sim$1–5 Myr.

Another independent way to estimate interstellar extinction is from photometry of field stars. The region around Monoceros R2 was studied in detail using 2MASS data by Lombardi et al. (2011) (Figure 4 in their paper), and the extinction to the V899 Mon location is $A_V = 2.6$ mag. This value is consistent with our previous color space analysis.

Figure 9 shows the position of V899 Mon in the $V/V-I$ optical CMD during various epochs. Siess et al. (2000) isochrones after correcting for extinction of $A_V = 2.6$ mag are also overplotted. Since the major component of the outburst phase flux is nonstellar in origin, the closest representation of the true position of V899 Mon might be its position during quiescent phase. The scatter forbids the estimation of age, but we get a rough estimate of the mass of V899 Mon as $2 M_\odot$. However, it should be noted that this estimate is sensitive to the estimated interstellar extinction value of $A_V = 2.6$ mag.
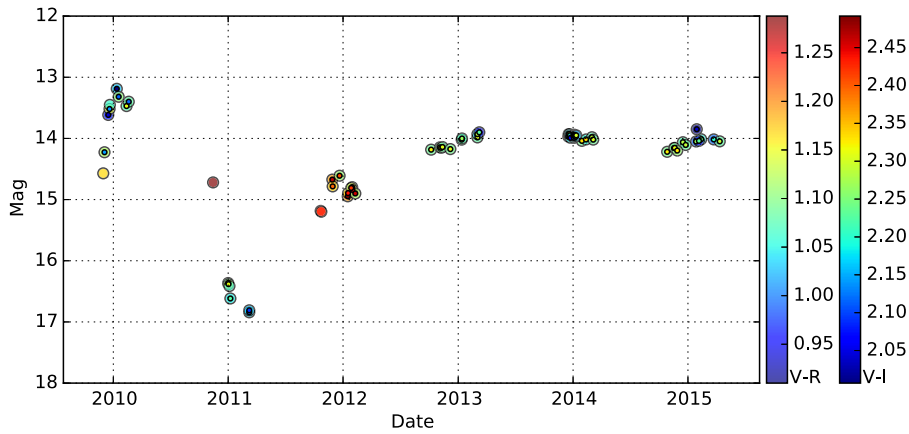
Figure 6. *V*-band light curve of V899 Mon showing evolution of its $V - R$ and $V - I$ colors. The color of the outer ring shows $V - R$, and the color at the center shows $V - I$. We see that both the colors were reddest during the transition from the quiescent phase to the outburst phase.

3.3. Spectral Energy Distribution

Flux estimates available of the V899 Mon over a wide wavelength range from optical to submillimeter were measured at random epochs. Since we had to use multiwavelength data of nearby epochs for the construction of the SED, we chose the epoch near the peak of the first outburst (2010 February–March), during which maximum observations were available. For fitting YSO SED models, we used the online SED Fitter tool by Robitaille et al. (2007). Flux estimates from both *IRAS* and PACS show that the flux of V899 Mon starts rising in the 90–200 μm range after a gradual drop of SED in the mid-infrared region (see Figure 10). No SED models in Robitaille et al. (2007) could fit this double-peaked SED. Possible scenarios of such an SED are discussed in Section 3.3.1. To avoid the second far-infrared peak while fitting the SED of V899 Mon, we used all the flux estimates above 90 μm as upper limits. For constraining the SED better we also used 70 μm flux measured during the second outburst in 2013, but to account for the change in 70 μm flux between two outbursts, we used a 1 Jy error bar (which is consistent with the flux change we have seen in 250 μm SPIRE data from two epochs). Figure 10(a) shows the SED fit obtained using *V, R, I, J, H, K$_S$, W1, W2, W3*, and *W4* fluxes from 2010 observations and PACS 70 μm flux from 2013 observations.

For fitting the SED of V899 Mon's quiescent phase, we used flux estimates from different quiescent phase epochs. Figure 10(b) shows the SED fit using *V, R, I*, 2MASS *J, H, K$_S$*, and *IRAS* 12 μm fluxes. MIPS1 (24 μm), PACS (70, 160 μm), and SPIRE (250, 350, 500 μm) fluxes were used only as upper limits.

Treating far-infrared PACS and SPIRE fluxes of 2013 to be a separate independent clump, we also fitted the SED by taking these fluxes alone (see Figure 11 and Section 3.3.2).

Stellar, disk, and envelope parameters obtained from all three SED fittings are tabulated together in Table 3.

3.3.1. 70 μm Dip in SED

The SED of V899 Mon shows a dip around 70–90 μm in both *IRAS* and PACS data taken at two different epochs. This shape of the SED is very unusual and not seen in any other FUors/EXors. Objects with extended circumstellar envelopes typically show a smooth flat SED. We also do not see heavy extinction in optical bands as expected from a source

surrounded by a large extended envelope. One possible scenario is that this object, instead of having a steady-state infall density distribution of the envelope, has a huge spherical cavity around it to a certain radius in the envelope. Significant optical light that we detect can be explained if our line of sight is along the opening created by the outflow.

Another possible geometric scenario is an envelope/clump with most of its mass behind V899 Mon. In the SPIRE 500 μm image (see Figure 12), we see that the bright blob marked with an ellipse at the position of V899 Mon is at the edge of a cloud, possibly being pushed back by the ionizing source of Monoceros R2.

We plan to carry out a detailed 3D radiative transfer modeling of such geometric structures to see whether this seemingly two-component SED can be explained.

3.3.2. Far-infrared Component Properties

Considering the far-infrared component part of the SED as a separate clump, we analyzed PACS-SPIRE data alone to obtain the characteristics of the clump. L_{bol} of the clump obtained by fitting the Robitaille et al. (2007) SED model for the far-infrared flux (>70 μm) is ~ 8.6 $L_{\odot}$ (Table 3).

We have SPIRE 250, 350, and 500 μm observations at two epochs: during the peak of the first outburst on 2010 September 4, and later during the second outburst in 2013 March 6. PACS 70 and 160 μm observations were available only during the second epoch. Photometric flux values estimated for V899 Mon from PACS and SPIRE data are given in Table 4. During the peak of the first outburst, fluxes were brighter than the second outburst by 2.8 Jy, 1.5 Jy, and 0.3 Jy in 250, 350, and 500 μm, respectively. V899 Mon was also optically brighter during the peak of the first outburst than the second outburst epoch by 0.75 mag (factor of 2) in *R* band. This implies that the far-infrared clump is heated by V899 Mon and is not spatially far from V899 Mon. We fitted the graybody model to SPIRE data from the two epochs (Figure 13) and estimated the mass to be 20 $M_{\odot}$ and temperature of the far-infrared clump to be 10.6 and 10.0 K at each epoch. This mass estimate is consistent with the envelope mass obtained from Robitaille et al. (2007) SED fitting (see Table 3). The graybody model was fitted using the

Figure 7. *V*, *R*, and *I* light curves of V899 Mon (circles, squares, and triangles, respectively), color-coded with the extinction-invariant color C_{VRI}.
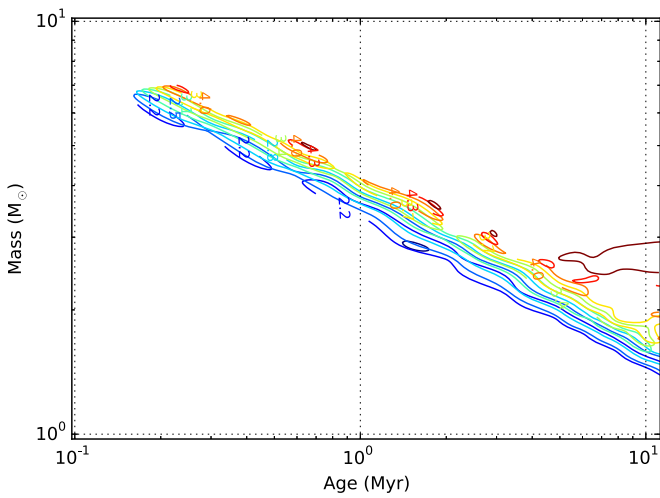
Figure 8. Contours showing 1σ constraints on mass and age of V899 Mon assuming Siess et al. (2000) isochrones to be a valid model for V899 Mon in four-dimensional $U - B$, $B - V$, $V - R$, and $R - I$ color–color space. Contours corresponding to a range of admissible reddening values A_V are shown in different colors, and the corresponding A_V is labeled on the contours.
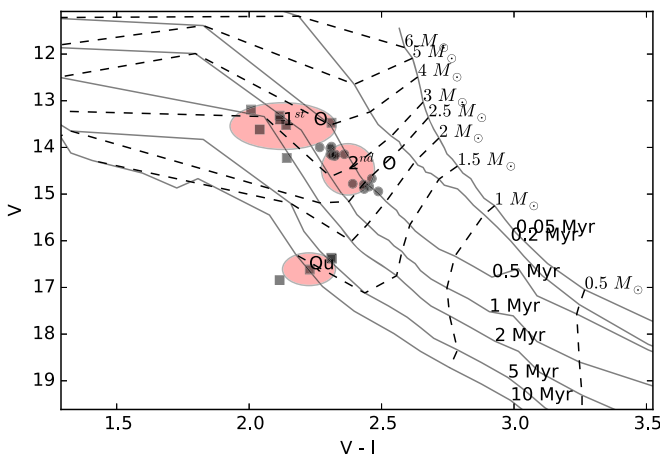
Figure 9. Optical $V/V - I$ color–magnitude diagram of V899 Mon during its first outburst (1st O), second outburst (2nd O), and quiescence (Qu) phases. Solid lines are Siess et al. (2000) isochrones corresponding to 0.05, 0.2, 0.5, 1, 2, 5, and 10 Myr. Dashed lines are evolutionary tracks of masses 0.5, 1, 1.5, 2, 2.5, 3, 4, 5, and 6 $M_\odot$. An extinction correction for an $A_V = 2.6$ mag and a magnitude correction for a distance of 905 pc are applied to all isochrones.

following formulation:

$$S_\nu(\nu) = \frac{M\left(0.01\left(\frac{\nu}{1000\text{ GHz}}\right)^\beta\right)B(T, \nu)}{D^2}, \qquad (1)$$

where $S_\nu(\nu)$ is the observed flux density, M is the mass of the clump, $B(T, \nu)$ is Planck's blackbody function for temperature T and frequency ν, D is the distance (taken to be 905 pc), and the dust opacity factor (κ_ν) was taken to be $0.01\left(\frac{\nu}{1000\text{ GHz}}\right)^\beta\,\text{m}^2\,\text{kg}^{-1}$, where β was fixed to be 2 (André et al. 2010).

To obtain a lower limit of A_V, we assumed that the entire mass M is in a uniform-density sphere of diameter $2R = 50''$ (FWHM of the source in the SPIRE 500 μm image), and then the mass column density to the center of the sphere should be $3M/(4\pi R^2)$. Since most of the gas is molecular, we can equate this column density to $N(\text{H}_2)\mu_{\text{H}_2}m_\text{H}$, where $N(\text{H}_2)$ is the H_2 column number density, μ_{H_2} is the mean molecular weight (taken to be 2.8), and m_H is the mass of hydrogen. Our mass estimate of $20\,M_\odot$ then corresponds to $N(\text{H}_2) = 4.6 \times 10^{21}$ molecules cm^{-2}. Using the relation $\langle N(\text{H}_2)/A_V \rangle = 0.94 \times 10^{21}$ molecules cm^{-2} mag^{-1} (Ciardi et al. 1998), we obtain an A_V to the center of the clump of 19.7 mag.

If we use PACS 160 μm flux also in the graybody fitting, then we obtain a mass of $12\,M_\odot$ and a temperature of the far-infrared clumps at the two epochs of 11.9 and 12.2 K. This mass corresponds to an $A_V = 10.7$ mag to the center of the uniform spherical clump. Both of these estimates are substantially higher than the actual A_V estimated from optical and NIR data. This implies that the heating source V899 Mon is not embedded at the center of this clump; it might be partially located on the front section of it (or any other geometry as discussed in Section 3.3.1). Even though the mass estimate has some systematic uncertainties from the distance, dust opacity factor, and graybody model assumption, they are unlikely to cause a difference of 8–15 mag in the A_V value.

3.4. Spectroscopic Results

V899 Mon has a rich spectrum of emission and absorption lines in optical and NIR. Figure 14 shows the flux-calibrated optical and NIR spectra taken during the second outburst phase of the source. Our spectroscopic observations in optical cover

(a) First outburst
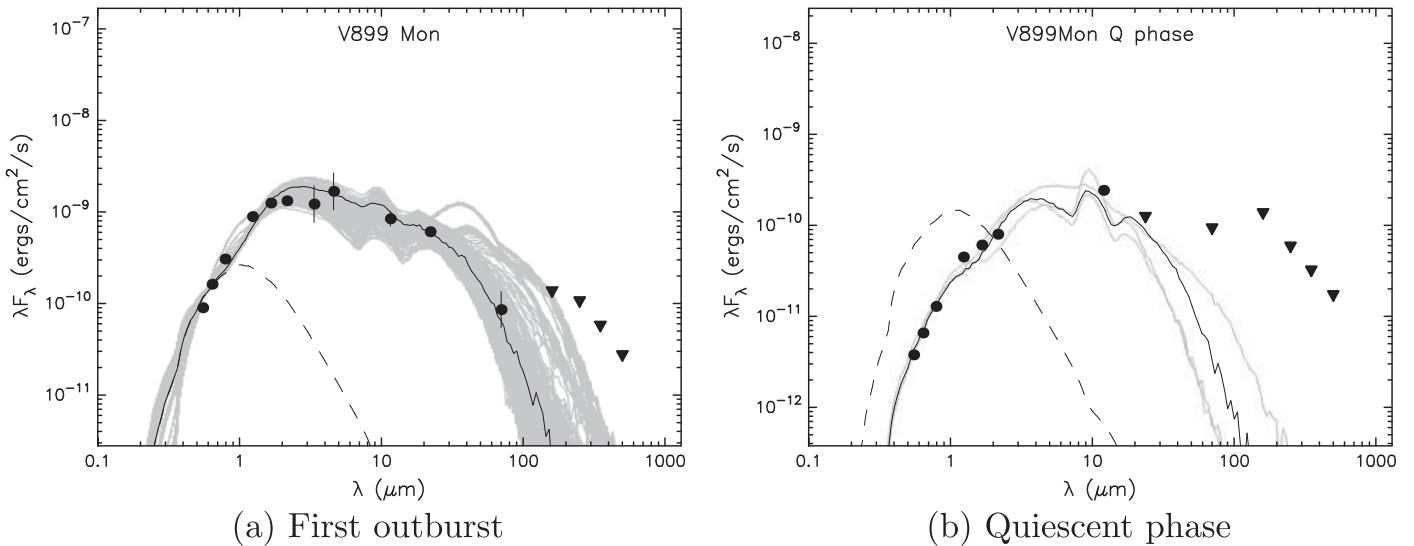
(b) Quiescent phase

Figure 10. SED fit of V899 Mon (a) during its peak of the first outburst using *V, R, I, J, H, K_S, W1, W2, W3,* and *W4* fluxes from 2010 and PACS 70 μm flux from 2013, (b) during its quiescent phase using *V, R, I,* 2MASS *J, H, K_S,* and *IRAS* 12 μm fluxes. MIPS1, PACS, and SPIRE fluxes were used only as upper limits. The filled circles represent the data points used for the fit, and filled triangles are upper limits. The solid black line is the best-fitted model, and the gray lines show subsequent good fits. The dashed gray line shows the stellar photosphere of V899 Mon in the best-fitted model (in the absence of circumstellar dust, but including interstellar extinction).
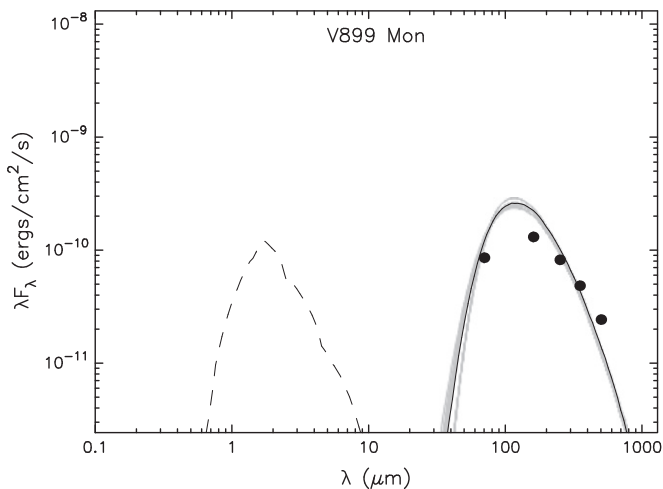
Figure 11. SED fit of V899 Mon during its second outburst phase using only *Herschel* PACS 70 and 160 μm and SPIRE 250, 350, and 500 μm fluxes. The filled circles represent the data points used for the fit. The solid black line is the best-fitted model, and the gray lines show subsequent good fits. The dashed gray line shows the stellar photosphere of V899 Mon in the best-fitted model (in the absence of circumstellar dust, but including interstellar extinction).

first outburst, transition, and quiescent phases, as well as the second outburst. The fluxes and equivalent widths of the detected lines at various epochs are tabulated in Table 5. The strong Ca II IR triplet emission lines in the spectrum confirm the V899 Mon source to be a YSO, and the detection of CO (2–0) and (3–1) bandhead absorption starting at 2.29 μm confirms this source to be an outburst family of FUors/EXors. These overtone bandhead lines are seen only in giants and FUors/EXors. In FUors/EXors they are believed to be forming in the accretion-heated inner regions of the disk, where temperature is in the range 2000 K < T < 5000 K and density $n_H > 10^{10}$ cm^{-3} (Kóspál et al. 2011). One notable line not detected in the V899 Mon spectrum is Brγ at 2.16 μm. While Brγ is typically found in strong accreting T Tauri stars, it is not detected in many FUors.

3.4.1. Extinction Estimates

To obtain de-reddened line fluxes, we need to know the extinction to the source. In Section 3.1 our NIR CC diagram does not show any significant extinction to the source. We also have an estimate of the interstellar extinction to the source of $A_V = 2.6$ mag from Figure 4 in Lombardi et al. (2011). Hα (6563 Å) and Hβ (4861 Å) lines show an emission component in their P Cygni profile. If we assume an optically thin case B emission, the Balmer decrement ratio of the Hα/Hβ emission component should be in the range of 2.8–3 (Osterbrock & Ferland 2006). Comparing this ratio with the ratios measured from our spectra, we obtained various estimates of A_V during outburst phase, ranging from 5.9 to 9.2 mag. Our Hβ profiles show a stronger absorption component than emission component; this might cause a significant underestimation of the Hβ flux, which was estimated by fitting a two-component Gaussian model to the line profile. This implies that the A_V estimate from the Balmer decrement is an overestimate. On the other hand, it is quite likely that the emission is not optically thin since it is believed to originate in the magnetospheric accretion column, which will make our estimate of A_V an underestimate. To be consistent with our other extinction estimates from the CC diagram and SED fitting in previous sections, we take A_V during the outburst phase to be 2.6 mag for the remaining spectral line calculations.

3.4.2. Accretion Rate

Many of the spectral line fluxes originating near the magnetosphere have been found to correlate with the accretion luminosity. The correlation is empirically calibrated in the simple form: $\log(L_{acc}/L_\odot) = a \log(L_{line}/L_\odot) + b$. For estimating accretion luminosity from hydrogen Balmer series, He I, O I, Ca II IR triplet, Paβ, and Paδ lines, we used the coefficients a and b from Alcalá et al. (2014). The distance to V899 Mon was taken to be 905 pc, and the observed fluxes were corrected for an extinction of $A_V = 2.6$ mag. To estimate the accretion

Table 3
SED Fit Results of V899 Mon

Parameter	Quiescence	First Outburst	Far-IR Alone
A_V (mag)	4.5 ± 1.1	4.2 ± 0.34	…
Distance (pc)	870 ± 80	794 ± 30	891 ± 55
Age_* (Myr)	4.84 ± 2.1	1.93 ± 1.8	$0.0073 \pm .002$
Mass_* ($M_\odot$)	3.7 ± 0.3	5.1 ± 0.5	0.57 ± 0.04
$\dot{M}_{\mathrm{envelope}}$ ($M_\odot$)	$0 \pm 5.7\mathrm{e}\text{-}09$	$0 \pm 7.9\mathrm{e}\text{-}08$	$24.7\mathrm{e}\text{-}05 \pm 2.4\mathrm{e}\text{-}05$
$\mathrm{Mass}_{\mathrm{Disk}}$ ($M_\odot$)	$1.2\mathrm{e}\text{-}05 \pm 0.0179$	$1.4\mathrm{e}\text{-}03 \pm 2.07\mathrm{e}\text{-}03$	0.048 ± 0.008
$\dot{M}_{\mathrm{disk}}$ ($M_\odot\,\mathrm{yr}^{-1}$)	$1.54\mathrm{e}\text{-}10 \pm 4.9\mathrm{e}\text{-}07$	$4.82\mathrm{e}\text{-}09 \pm 7.6\mathrm{e}\text{-}08$	$5.48\mathrm{e}\text{-}07 \pm 2.7\mathrm{e}\text{-}07$
L_{total} ($L_\odot$)	162 ± 79	419 ± 168	8.55 ± 1.54
$\mathrm{Mass}_{\mathrm{env}}$ ($M_\odot$)	$8.13\mathrm{e}\text{-}08 \pm 0.027$	$1.52\mathrm{e}\text{-}05 \pm 0.07$	23.43 ± 2.0

Note. Median and standard deviation of the best-fitted 20 models in each case.
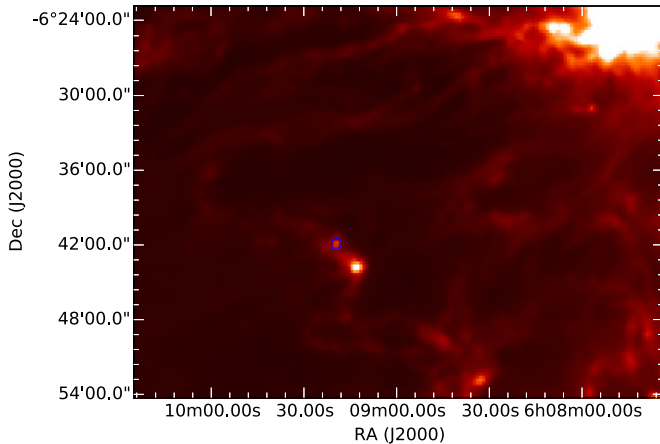
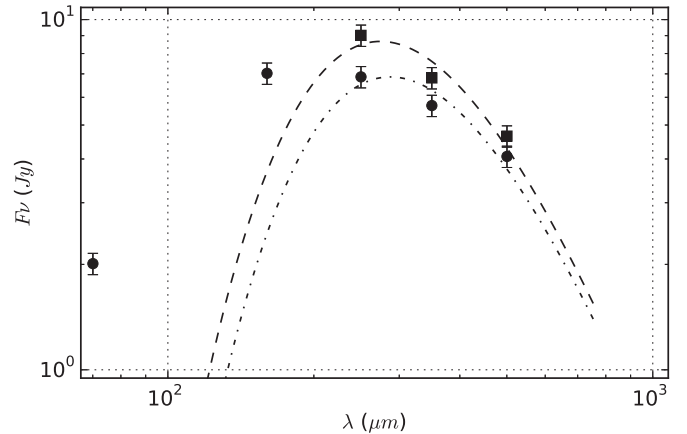**Figure 12.** SPIRE 500 μm image of the V899 Mon field taken on 2013 March 16. The location of V899 Mon is marked with an ellipse to show the major and minor FWHM sizes determined for V899 Mon by the source extraction algorithm *getsources* (Men'shchikov et al. 2012). The brighter source IRAS 06068–0643, southwest of V899 Mon, is also a more embedded outburst source. The bright blob in the northwest corner of the image is the ionizing source in Monoceros R2.


Figure 13. Graybody fit of V899 Mon's far-infrared SPIRE wavelength fluxes at two epochs. Filled squares are from the 2010 epoch during the peak of the first outburst, and filled circles are from 2013 during the second outburst. The dashed line is the graybody fit to the SPIRE data points of the first outburst in 2010, and the dot-dashed line is the fit to the SPIRE data points observed in 2013 during the second outburst. PACS data points of the second epoch are also shown, but were not used for the graybody fit.

Table 4
Far-infrared Fluxes of V899 Mon

Band	2010 Sep 14	2013 Mar 06	Δ Flux
PACS 70 μm	…	2.01 Jy	…
PACS 160 μm	…	7.02 Jy	…
SPIRE 250 μm	9.02 Jy	6.86 Jy	2.86 Jy
SPIRE 350 μm	6.82 Jy	5.68 Jy	1.48 Jy
SPIRE 500 μm	4.65 Jy	4.06 Jy	0.33 Jy

Note. Δ flux between two epochs was estimated by aperture photometry on difference images using apertures 48″, 60″, and 70″ for 250, 350, and 500 μm, respectively.

rate from the accretion luminosity, we assumed a mass and age of V899 Mon of $2.5\,M_\odot$ and 1 Myr, respectively (consistent with the CMD). Stellar radius was then estimated to be $4\,R_\odot$ based on the isochrone for these values of mass and age (Siess et al. 2000). Finally, using the formula $\dot{M}_{\mathrm{disk}} = (L_{\mathrm{acc}} R_* / GM)(1 - R_*/R_i)^{-1}$ (where disk inner radius $R_i \sim 5 \times R_*$; Gullbring et al. 1998), we obtained accretion rates from various lines along the spectrum. No veiling correction was done for lines that are in absorption; hence, these accretion rate estimates can be slight underestimates. Figure 15 shows all the estimates of accretion rates

from various lines as a function of their wavelengths. Figure 16 shows the normalized accretion rates obtained from different lines at various epochs. A clear reduction in relative accretion, by at least a factor of 2 during quiescent phase with respect to the second outburst phase, is seen in all the accretion rates obtained from different lines.

3.4.3. Mass Loss

Ratio of the mass loss to mass accretion in YSOs is a key parameter predicted by various jet launch mechanism models. The FUors/EXors family of objects gives us a direct observational constraint on this ratio. Based on the SED fit in Section 3.3, we obtained an L_{bol} of V899 Mon of $\sim 150\,L_\odot$ during the outburst phase. Using the relation between mass loss and L_{bol} in young HeBe and T Tauri stars, viz., $\log(\dot{M}) = -8.6 + 0.7 \times \log(L_{\mathrm{bol}})$ by Nisini et al. (1995), we get an estimate of the mass outflow in V899 Mon of $1 \times 10^{-7}\,M_\odot\,\mathrm{yr}^{-1}$. This rate is larger than typical T Tauri stars ($10^{-8}\,M_\odot\,\mathrm{yr}^{-1}$) but less than classical FUors ($10^{-5}\,M_\odot\,\mathrm{yr}^{-1}$) (Hartmann & Kenyon 1996).

We could also directly measure the mass-loss rate from [O I] $\lambda 6300$ flux using the relation *A8* of Hartigan et al. (1995). Mass outflow is directly proportional to the optically thin forbidden line emission fluxes originating in outflow. The
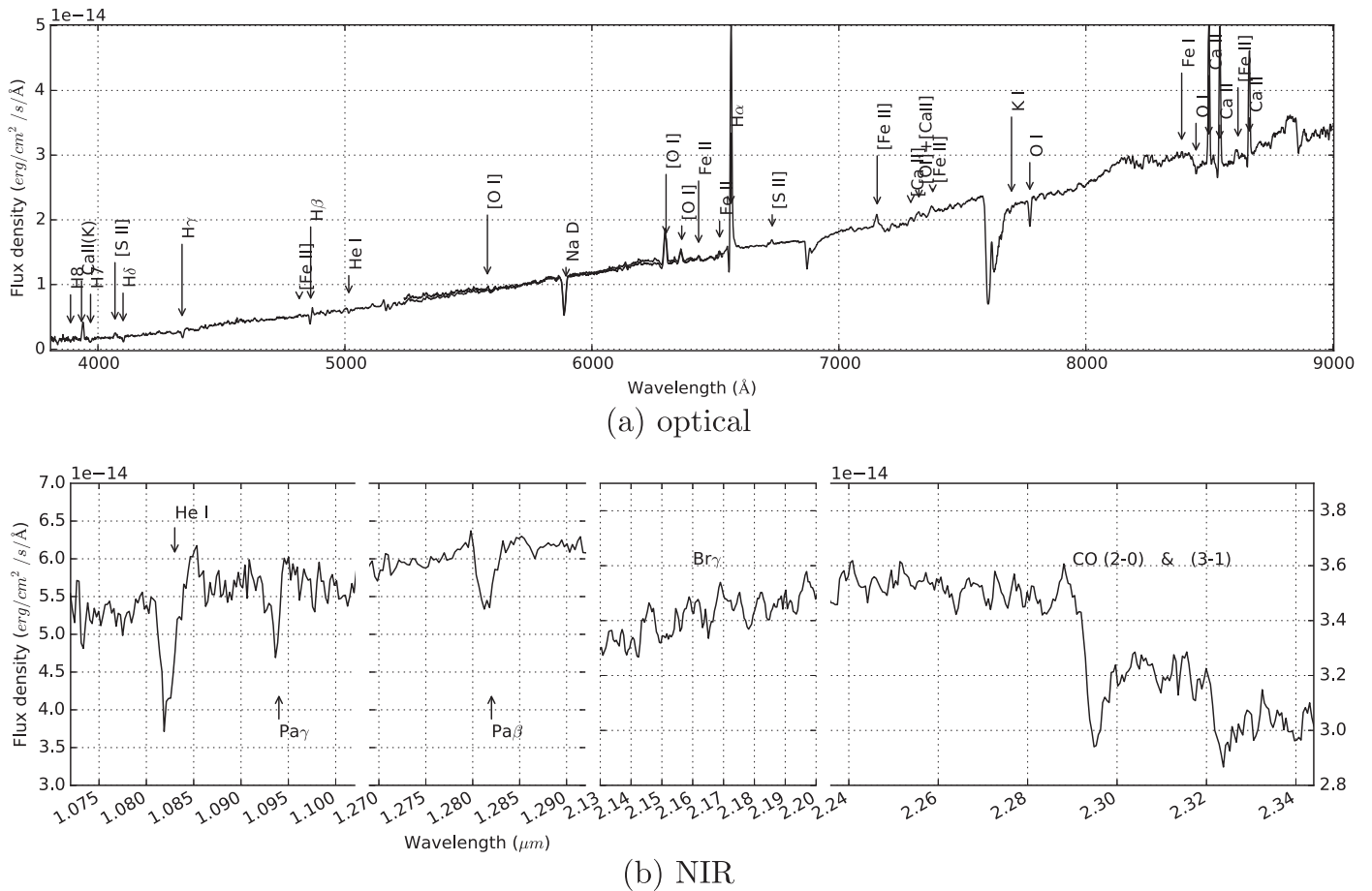
Figure 14. Flux-calibrated optical and NIR spectra of V899 Mon during its second outburst. All spectra observed during the second outburst were median combined to improve signal-to-noise ratio. Identified lines in the spectra are labeled. The optical spectrum (a) is not corrected for atmospheric absorption lines. The absorption lines that are not labeled in the optical spectrum are atmospheric lines.

mass-loss estimate from [O I] $\lambda6300$ flux through a 2″ slit aperture, by assuming a distance of 905 pc and a typical sky plane component of the outflow velocity of 150 km s^{-1}, is $2.6 \times 10^{-7} M_\odot$ yr^{-1}.

We could not detect any significant change in these forbidden line fluxes during quiescence. Our 2″ slit aperture at 905 pc distance corresponds to a 2.7×10^{11} km wide region. Even if we assume the sky plane velocity to be as large as 700 km s^{-1} (seen in P Cygni outflow), the gap in outflow due to 1 yr of quiescence will be only 2.2×10^{10} km, which is just 1/10 of the total aperture. Hence, our nondetection does not conclude whether the large-scale low-density outflow traced by forbidden lines was interrupted or remained uninterrupted during the quiescence phase.

3.4.4. Outflow Temperature and Density

Flux ratios of the optically thin forbidden emission lines provide a direct estimate of the density and temperature of the outflow region. For better signal-to-noise ratio, we estimated the average flux of the forbidden lines by combining all the second outburst phase spectra of V899 Mon. Flux ratio [S II] $\lambda6716/\lambda6731$ is a good tracer of density and is insensitive to temperature. Flux of the [S II] $\lambda6731$ line is 2.4×10^{-14} erg cm^{-2} s^{-1}, whereas the [S II] $\lambda6716$ line is not detected in our spectrum, so we estimate the upper limit to be $<1 \times 10^{-14}$ erg cm^{-2} s^{-1}. The ratio [S II] $\lambda6716/\lambda6731 < 0.45$ implies that the electron density n_e is $>10^4$ cm^{-3} (Figure 5.8 in Osterbrock & Ferland 2006). Th ratio of [O I] $\lambda5577/\lambda6300$ in V899 Mon is ~0.09. For a range of temperature from 9000 to 20,000 K, this ratio is consistent with n_e ranging from 2×10^5 cm^{-3} to 4×10^6 cm^{-3} (Figure 6 in Hamann 1994).

Once we have a density constraint, we can now use other line ratios to estimate the temperature. For instance, using the formula 5.5 in Osterbrock & Ferland (2006), for a density of $n_e = 2 \times 10^5$ cm^{-3}, ratio [O I] $(\lambda6300+\lambda6364)/\lambda5577 \sim 15$ gives an estimate on the temperature of ~8500 K. Density-insensitive line ratio [Ca II] $\lambda7291/$[O I] $\lambda6300 \sim 0.1$ in V899 Mon implies a temperature <9000 K (Figure 5 in Hamann 1994). But the line ratio [S II] $\lambda6731/$[O I] $\lambda6300 \sim 0.08$ implies a temperature >9000 K (Figure 5 in Hamann 1994). To be consistent with all these independent estimates, we shall take the temperature of the outflow to be ~9000 K.

3.4.5. Line Profiles and Variability

3.4.5.1. Hα λ6563

Almost all prominent lines in the spectrum showed variability during our period of observations. The line that showed the most dramatic changes in line profile is Hα, which has a strong P Cygni absorption component and is believed to be formed in a magnetospheric accretion funnel. Figure 17

Table 5
Spectral Line Measurements

Date	JD	$H\alpha$ $\lambda6562.8$				Ca II $\lambda8498$	
		eqw (Å)	Flux (erg cm^{-2} s^{-1})	eqw$_{abs}$ (Å)	Outflow Velocity (km s^{-1})	eqw (Å)	Flux (erg cm^{-2} s^{-1})
2009 Nov 30	2,455,166.33	−17.5	1.9e-13	…	…	−10.1	1.52e-13
2009 Dec 17	2,455,183.21	−6.88	1.38e-13	4.27	−254	−3.7	1.21e-13
2009 Dec 21	2,455,187.27	−7.77	1.83e-13	7.17	−199	−4.78	1.74e-13
2009 Dec 29	2,455,195.22	−6.82	1.69e-13	2.48	−263	−4.7	1.89e-13

Note. Online version contains data of 28 lines.

(This table is available in its entirety in machine-readable form.)
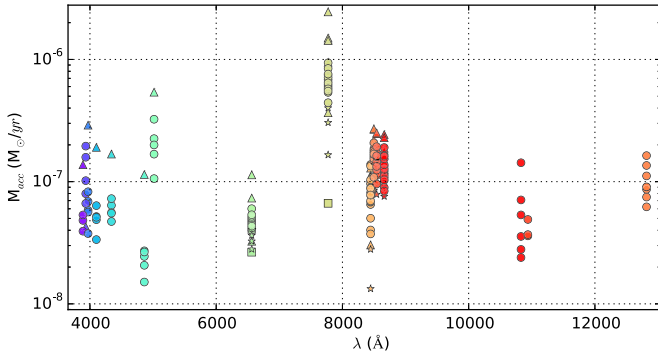
Figure 15. Accretion rates estimated from various lines from V899 Mon's optical and NIR spectra. Triangles show the first outburst phase, squares show the quiescent phase, stars show the transition phase, and circles show the second outburst phase. There is a significant difference in accretion rates estimated using different lines.

shows the evolution of the $H\alpha$ P Cygni profile during its first outburst phase, quiescent phase, and the current ongoing second outburst phase. It is a selected representative sample of line profile plots from each epoch. The first spectrum published by Wils et al. (2009) shows no P Cygni profile in $H\alpha$. Our initial spectrum observed 13 days later during the peak of first outburst shows a CI Tau profile typically seen in many T Tauri stars (Stahler & Palla 2005). In subsequent spectra, the absorption component grows considerably, transforming the $H\alpha$ line profile into a strong P Cygni profile (Figure 17). We also see complex structures in the absorption component of P Cygni in the spectrum taken on 2010 January 17. All these evolutions indicate that the outflow wind increased dramatically toward the end of first outburst. By the onset of the quiescent phase, the absorption component in P Cygni completely disappears and the $H\alpha$ shows a near-symmetric emission line. We also do not see any P Cygni profile when the source was undergoing transition from the quiescent phase to the second outburst phase. P Cygni profiles, much fainter in strength compared to the peak of the first outburst, only start appearing after the full onset of the second outburst. Even though during the second outburst the outflow P Cygni profile is more stable than during the last phase of the first outburst, the spectrum taken on 2014 September 25 shows only a very weak P Cygni in $H\alpha$. These delays and short pauses indicate a nonsteady nature in the outflows from FUors/EXors. Table 5 shows the fluxes and equivalent widths obtained by fitting a two-component Gaussian to the line profiles. Our high-resolution spectrum ($R \sim 37,000$) taken using SALT-HRS on 2014 December 22 resolves the $H\alpha$ line and its multi-component profile. Figure 18(a) shows the emission component
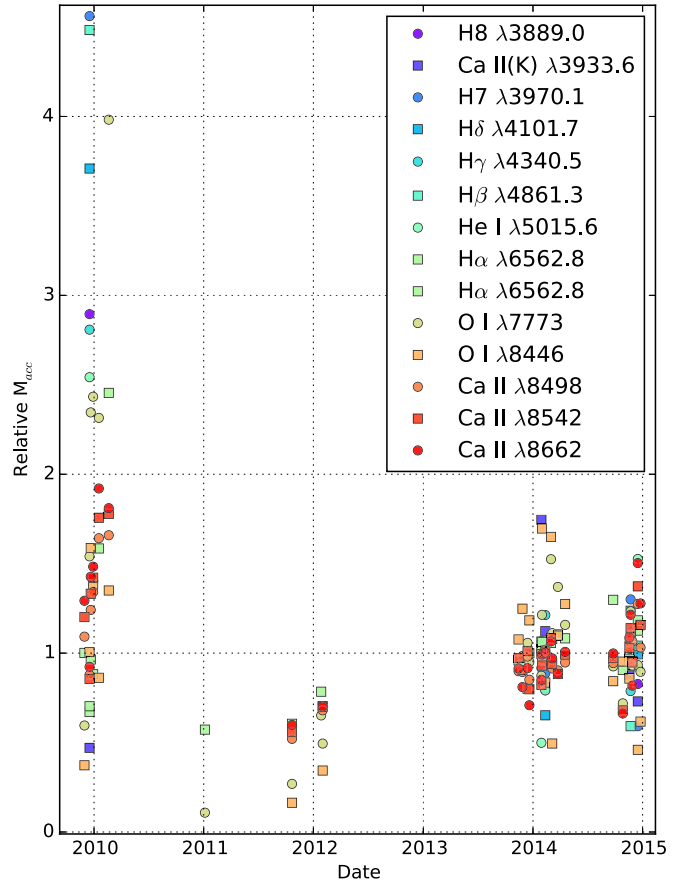
Figure 16. Relative change in accretion rates estimated from various lines during the transition from the first outburst phase to the quiescent phase and back to the second outburst.

of the $H\alpha$ line profile, and Figure 18(b) shows the absorption component in the spectrum taken using SALT-HRS. The redshifted part of the profile peaks at $+18 \, \mathrm{km \, s^{-1}}$ and has smooth wings with an extra broad component reaching up to a velocity of $+420 \, \mathrm{km \, s^{-1}}$ (Figure 18(a)). On the other hand, the blue part of the profile shows complicated multicomponent velocity structures (Figure 18(b)). The outflow absorption component extends up to $-722 \, \mathrm{km \, s^{-1}}$. We could see structures in absorption at -648, -568, -460, -274, -153, -100, and $-26 \, \mathrm{km \, s^{-1}}$. These are typically associated with bulk motion within the outflowing gas (Stahler & Palla 2005). To understand how the outflow components evolve, it will be interesting to study the evolution of these components in
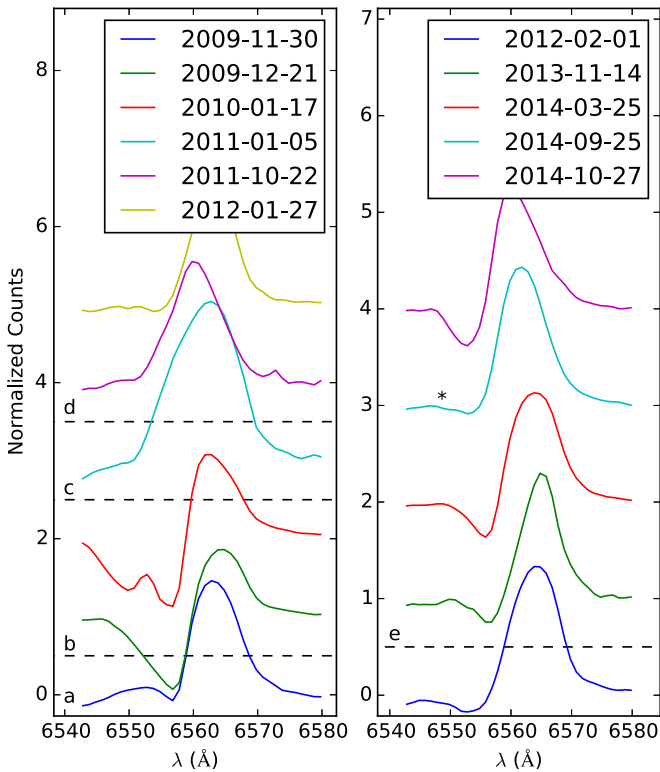
Figure 17. Selected sample of Hα emission line profiles from different phases of V899 Mon. (a) First outburst phase; (b) heavy outflow during the end of first outburst phase; (c) quiescent phase; (d) transition phase from quiescence phase to second outburst phase; (e) second outburst phase. The asterisk indicates a particular profile on 2014 September 25, when the P Cygni became very weak for a very short duration. The spectrum taken immediately after 1 month shown in the top of the right panel had a strong P Cygni profile.

velocity time space by carrying out multiepoch high-resolution spectroscopic observations.

3.4.5.2. Forbidden lines [O I] λ6300, λ6363, [Fe II] λ7155

Another important tracer of outflow is the forbidden line [O I] at 6300.304 Å. Our medium-resolution time evolution study does not show significant variation in this line, possibly owing to the fact that they originate in low-density jets/ outflows. The SALT-HRS high-resolution spectrum shows a very interesting plateau profile for the [O I] λ6300.3 line (see Figure 19 for the resolved profile). Since we have not corrected our spectrum for telluric absorption, we shall not interpret the narrow absorption dips seen on the plateau structure. The profile has a strong redshifted emission at $+25$ km s^{-1} with an FWHM of 21 km s^{-1}. The emission in the blueshifted part extends up to ~ -450 km s^{-1}. Figure 20 shows the other two weaker forbidden lines [O I] λ6363 and [Fe II] λ7155 plotted over the [O I] λ6300 profile. We see an almost similar structure in [O I] λ6363.8, with a blueshifted emission extending up to -450 km s^{-1} and a narrow peak emission at $+20$ km s^{-1}. The [Fe II] λ7155 line also shows a very similar structure with a blue part extending up to ~ -500 km s^{-1} and a peak emission at $\sim +22$ km s^{-1}. Since the forbidden line emissions are optically thin, their flux is directly proportional to the column density of emitting species. The plateau profile implies almost equal column density in the blueshifted outflow with a velocity gradient in the jet. Since we are detecting only the velocity component of the jets along the line of sight, the gradient can

be either due to actual change in the outflow velocity or due to the geometrical projection effect of the outflow. A cone-shaped outflow in the direction of the observer can give rise to different projected velocities from different radial regions of the cone. A time evolution study of these profiles will give insight into the structure of the outflow. The redshifted emission peak is more difficult to explain. This might be originating from the envelope to disk infall shock regions on the surface of the disk, or from the tail part of a bipolar outflow that is moving away from us and emerging out of the region occulted by the disk in our line of sight.

3.4.5.3. Ca II IR Triplet λ8498, λ8542, λ8662

Ca II IR triplet lines (λ8498.02, λ8542.09, λ8662.14) are believed to be originating inside and very near to the accretion column, resulting in their tight correlation with accretion rate (Muzerolle et al. 1998). Our continuous spectral monitoring shows that the P Cygni profile in Ca II IR triplet lines evolved similar to Hα. The outflow component got stronger toward the end of the first outburst, then completely disappeared during the quiescent phase, and finally reappeared after the full onset of the second outburst. As seen in typical T Tauri stars and FUors/EXors, the line ratios of Ca II IR triplet lines in the V899 Mon spectrum are found to be 1:1.01:0.77, representing an optically thick gas dominated by collisional decay. Unlike the emission components, the ratio of P Cygni absorption components of λ8542 and λ8662 measured from the high-resolution spectrum is 0.83:0.53 (=1.57:1), which is more consistent with atomic transition strengths (1.8:1). This implies that the absorption components in outflow are optically thin. These values are surprisingly similar to the P Cygni profiles of Ca II IR triplet lines detected in the episodic winds of V1647 Ori (Ninan et al. 2014). Following the same arguments as in Ninan et al. (2014), we could estimate the Ca II column density in the outflow to be 3.4×10^{12} cm^{-2} and the hydrogen column density $N_{\rm H} \sim 3.8 \times 10^{20}$ cm^{-2}.

Figure 21 shows the resolved profiles of Ca II IR triple lines. All three triplet lines (λ8498.02, λ8542.09, λ8662.14) show an asymmetric triangular profile with a steeper slope on the red side and a shallower slope on the blue side. The peaks of these lines are redshifted by $+18.7$, $+21.4$, and $+23.2$ km s^{-1}, respectively. This increase in the redshift is also seen in the line center estimated by fitting a Gaussian profile to the lines. The σ of the fitted Gaussian for each line is 1.177, 1.229, and 1.186 Å, respectively. The ratio of line widths of λ8498 and λ8542 is 0.96, which implies that λ8498 is $\sim 4\%$ thinner than λ8542, as seen in many other T Tauri stars (Hamann & Persson 1992), though there is no statistically significant evidence for the peak of the former line to be larger than the latter one. Hamann & Persson (1992) attributed these ratios to substantial opacity broadening of λ8542 or to lower dispersion velocity in the deeper part of the region from where Ca II IR triple lines originate. The velocities of the smooth broadened emission profiles extend up to ± 150 km s^{-1}. Figure 22 shows the P Cygni absorption component in Ca II λ8542 and λ8662 lines. The absorption components are quite broad and extend up to ~ -470 km s^{-1} in both lines. The absorption component in λ8662 shows a prominent structure that extends only up to ~ -250 km s^{-1}.
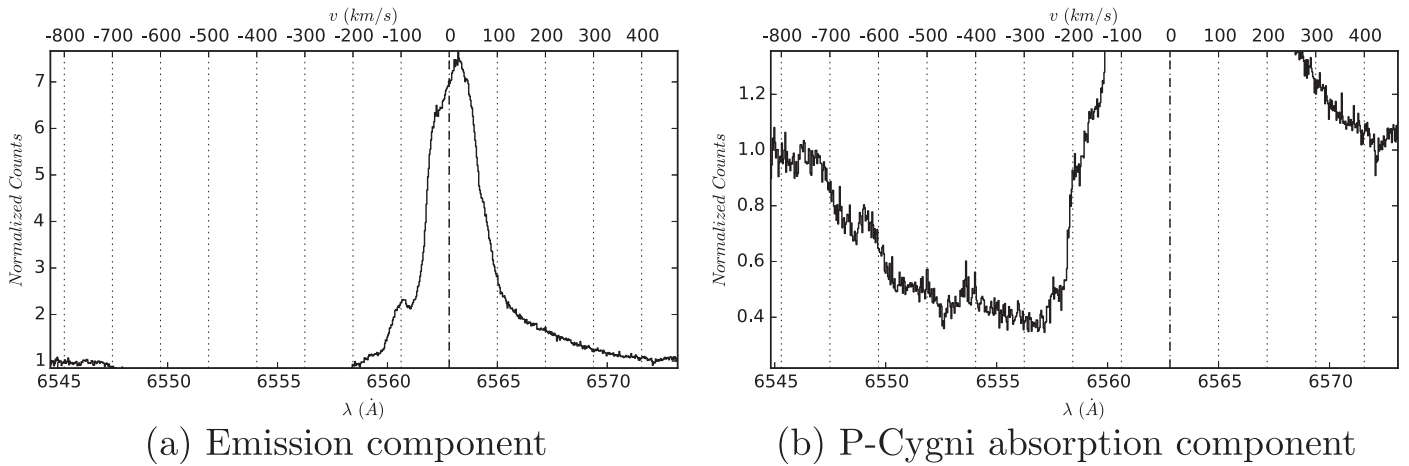
Figure 18. Hα (a) emission and (b) P Cygni absorption line profiles of V899 Mon observed on 2014 December 22 using SALT-HRS.

3.4.5.4. O I λ7773, λ8446

The absorption component of O I triplet lines at 7773 Å (Figure 23), which is not seen in the photosphere of cool stars, is believed to be formed in T Tauri stars owing to warm gas in the envelope or hot photosphere above the disk, and it is an indicator of the turbulence (Hamann & Persson 1992). The equivalent widths of this line in V899 Mon spectra show a very strong increase and then sudden decrease in strength just before the source went into the quiescent phase (see Figure 24). Owing to turbulence or disk rotational broadening of the O I triplet lines at 7771.94, 7774.17, and 7775.39 Å, our high-resolution spectrum (see Figure 23) shows a blended Gaussian absorption profile with $\sigma = 2.43$ Å (FWHM = 220 km s^{-1}). The velocities originating from turbulence or disk rotation extend up to $\sim\pm200$ km s^{-1}.

Another O I triplet at λ8446 (containing λ8446.25, λ8446.36, λ8446.76 triplet lines) is also seen in absorption in our SALT-HRS spectrum. These lines are also blended and have a combined FWHM = 174 km s^{-1}. The central position of the absorption line does not show any significant redshift and if present can be constrained to be <5 km s^{-1}. This implies that the $\sim$+20 km s^{-1} (heliocentric velocity) redshift component seen in emission line profiles like the Ca II IR triplet and forbidden lines are not due to any uncorrected peculiar velocity of V899 Mon with respect to our Sun.

3.4.5.5. Fe I λ8514, λ8387, λ8689, λ8675

Many Fe I emission lines were detected in our medium-resolution optical spectrum. All these lines were also resolved in SALT-HRS spectrum. Fe I λ8514 is a blend of two lines at 8514.07 and 8515.11 Å; their blended profile has an FWHM of 76 km s^{-1}. Fe I λ8387.777 has a +26.5 km s^{-1} redshifted profile with an FWHM of 62.8 km s^{-1}, Fe I λ8688.625 has a +26.74 km s^{-1} redshifted profile with an FWHM of 63.3 km s^{-1}, whereas a weaker Fe I λ8674.746 line has a +40 km s^{-1} redshifted profile with an FWHM of 59.2 km s^{-1}. The redshifts in these lines are consistent with the redshifts we have measured in other resolved lines (for example, in Ca II IR triplet lines and forbidden lines).

3.5. Constraints from 1280 MHz Observation

V899 Mon was not detected in the 1280 MHz GMRT radio continuum map observed during its second outburst. The local background noise σ in the map after cleaning was $\sim$0.1 mJy. We could detect eight other point sources in the $28' \times 28'$ FOV map centered at V899 Mon's position. For this study, we take a $5\sigma \sim 0.5$ mJy to be a strict upper limit on V899 Mon's 1280 MHz flux.

The ionizing flux from the magnetospheric accretion can create an H II region around the central source. Even though hydrogen Balmer lines detected in our optical spectra originate in the ionized region, since they are not optically thin, we cannot use them to constrain the extent of the H II region.

If we consider the H II region to be formed by a smooth, isothermal and isotropic stellar outflow, from our mass outflow rate and velocity estimates, we can obtain the expected flux using the following formula (Moran 1983):

$$S(\nu) = 1.3\left(\frac{T_e}{10^4\,\mathrm{K}}\right)^{0.1}\left(\frac{\dot{M}}{10^{-6}M_\odot\,\mathrm{yr}^{-1}}\right)^{4/3}$$
$$\times \left(\frac{v}{10^2\,\mathrm{km\,s}^{-1}}\right)^{-4/3}\left(\frac{D}{\mathrm{kpc}}\right)^{-2}\left(\frac{\nu}{\mathrm{GHz}}\right)^{0.6}\mathrm{mJy},$$

where $S(\nu)$ is the expected flux density, T_e is the electron temperature of the outflowing ionized wind, $\dot{M}$ is the mass outflow rate, v is the terminal velocity of outflow, D is the distance to V899 Mon, and ν is the frequency of observation. From our spectroscopic estimates of these quantities, we can substitute $\dot{M} = 0.26 \times 10^{-6}\,M_\odot\,\mathrm{yr}^{-1}$, outflow velocity $v = 1.5 \times 10^2$ km s^{-1}, $T_e = 0.9 \times 10^4$ K, $D = 0.905$ kpc, and $\nu = 1.28$ GHz. We obtain $S(1.28\,\mathrm{GHz}) = 0.17$ mJy, which is consistent with our observed upper limit of 0.5 mJy. Since the outflows we detected in the optical spectrum are unlikely to be an isotropic outflow, our predicted estimate of 0.17 mJy is also an upper limit.

Instead of considering a radial density profile due to outflow, since we have an estimate of density from forbidden optical lines, we can calculate an upper limit on the maximum size of a homogeneous, isotropic, spherical H II region around V899 Mon. For an H II region of radius R_s, using a spherical volume
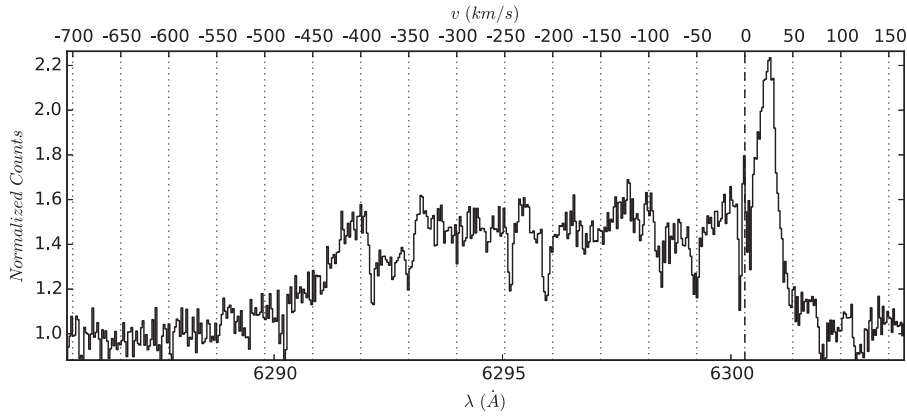
Figure 19. [O I] $\lambda6300$ emission line structure from V899 Mon observed on 2014 December 22 using SALT-HRS.
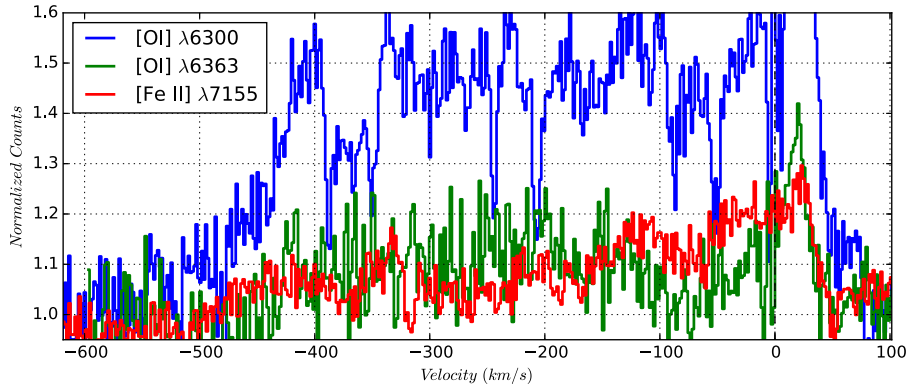
Figure 20. [O I] $\lambda6363$ and [Fe II] $\lambda7155$ emission line profile structures plotted over the [O I] $\lambda6300$ profile of V899 Mon observed on 2014 December 22 using SALT-HRS.

emission measure, we have the expression (Moran 1983)

$$S(\nu) = 3.444 \times 10^{-83} \left(\frac{10^4 \text{ K}}{T_e} \right)^{0.35}$$
$$\times \left(\frac{1 \text{ GHz}}{\nu} \right)^{0.1} \left(\frac{1 \text{ kpc}}{D} \right)^2 \frac{4\pi R_s^3}{3} n_e^2$$

where the radius of the H II region R_s is in cm, and electron density n_e is per cm^3. Taking 0.5 mJy as an upper limit on $S(\nu)$ and $n_e \sim 1 \times 10^6$ cm^{-3}, we obtain $R_s < 20$ AU. Since the flux of the ionizing Lyman continuum inside an H II region is equal to the volume emission measure times the recombination rate, we have obtained the following relation for N_{Lyc}:

$$N_{\text{Lyc}} = 7.5487 \times 10^{43} \times \left(\frac{S(\nu)}{\text{mJy}} \right) \left(\frac{T_e}{10^4 \text{ K}} \right)^{-0.45}$$
$$\times \left(\frac{\nu}{1 \text{ GHz}} \right)^{0.1} \left(\frac{D}{1 \text{ kpc}} \right)^2.$$

Using our upper limit of $S(\nu)$, we obtain an upper limit on the Lyman continuum flux from V899 Mon of $N_{\text{Lyc}} < 5 \times 10^{43}$ photons s^{-1}.

4. DISCUSSION

4.1. Cause of Break in the First Outburst

According to standard instability models of FUors/EXors, a critical disk surface density is required to sustain the instability.

Disk transition occurs from outburst phase to quiescent phase when its surface density drops below that critical value (Bell & Lin 1994; Zhu et al. 2009). Since the effective viscosity of the disk is lower during the quiescent phase than the outburst phase, the surface density increases more slowly during the quiescence than the rate at which it drained during the last outburst phase. Particularly in the case of V899 Mon when the first outburst stopped, if the disk density had drained below the critical density, then it has to spend more time in the subsequent quiescent phase to replenish the disk before undergoing a second outburst. Such a scenario is also seen in the light curve of another famous and very similar FUor candidate, V1647 Ori (Ninan et al. 2013). V582 Aur (FUor source) also showed multiple very brief quiescences during the ongoing outburst (Semkov et al. 2013). In order to explain these short-duration breaks in outbursts, we need to look for mechanisms during an outburst that can pause the accretion for a short duration before the disk gets critically drained. In such scenarios, the outburst can re-initiate as soon as the mechanism that was pausing the accretion disappears.

The average rate of change in V899 Mon's magnitude during the onset of first outburst was 0.038 mag month^{-1}; on the other hand, during the onset of second outburst it was larger than 0.15 mag month^{-1}. This difference implies that the timescales of the mechanisms that triggered the first and second outbursts are different.

Before V899 Mon transitioned to the quiescent phase, its spectroscopic observations showed an increase in the outflow activity (Section 3.4). Later the strong P Cygni profiles of

(a) $\lambda 8498$

(b) $\lambda 8542$

(c) $\lambda 8662$
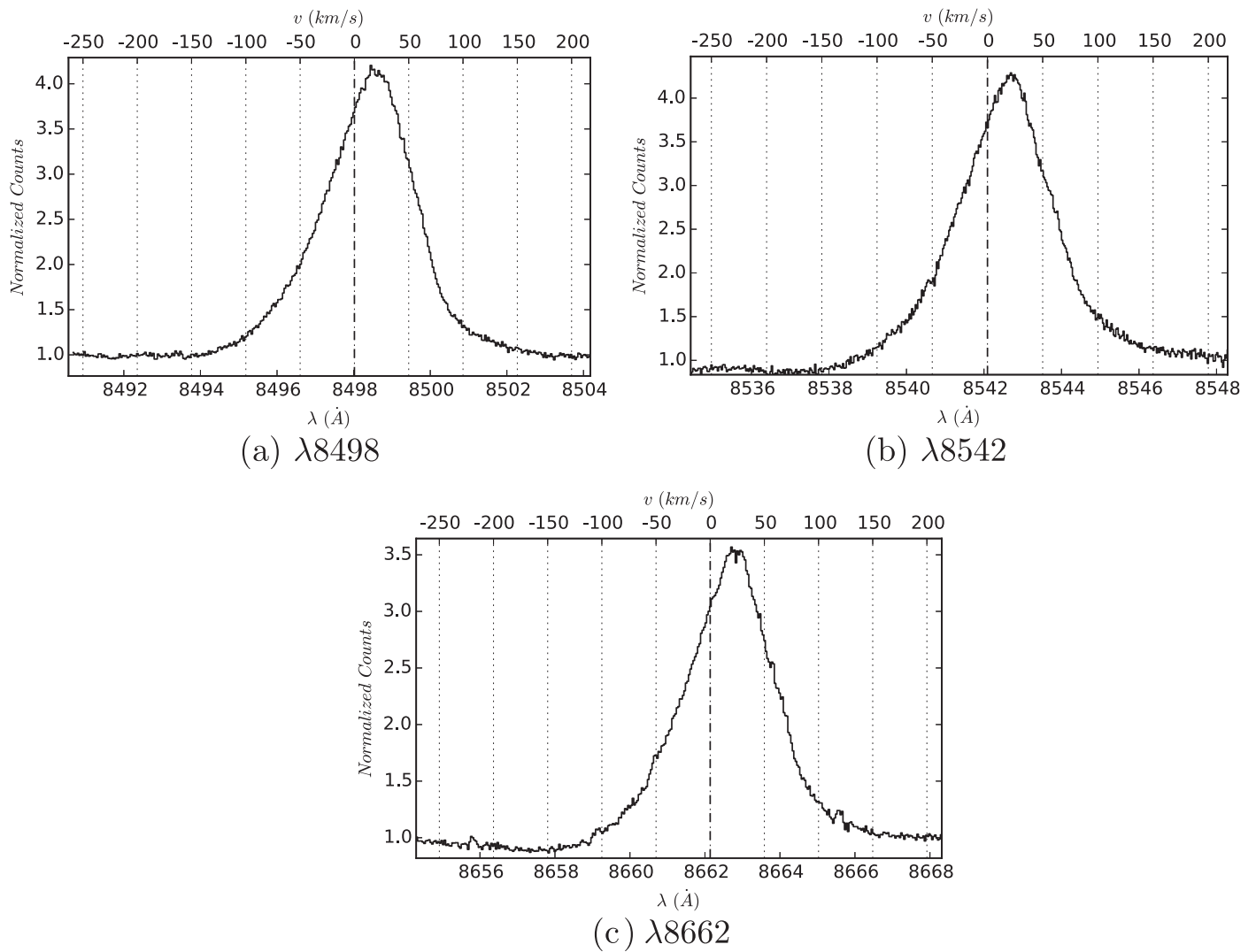
Figure 21. Ca II IR triplet emission line profiles of V899 Mon observed on 2014 December 22 using SALT-HRS.

(a) $\lambda 8542$


(b) $\lambda 8662$
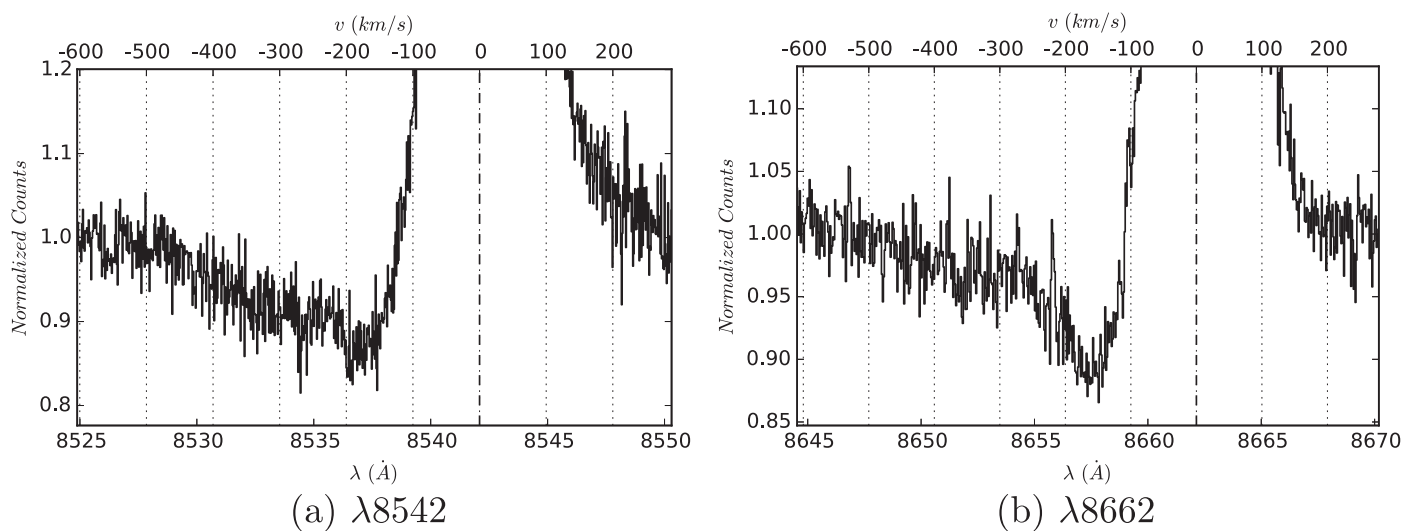
**Figure 22.** Ca II IR triplet P Cygni absorption line profile of V899 Mon observed on 2014 December 22 using SALT-HRS.

outflow suddenly vanished as the object entered the quiescent phase. Since outflows are believed to be driven by magnetic fields, it is possible that some magnetic-field-related mechanism is responsible for abruptly pausing the accretion during the active outburst phase. Spectral line fluxes that are proportional to accretion, as well as the continuum flux of
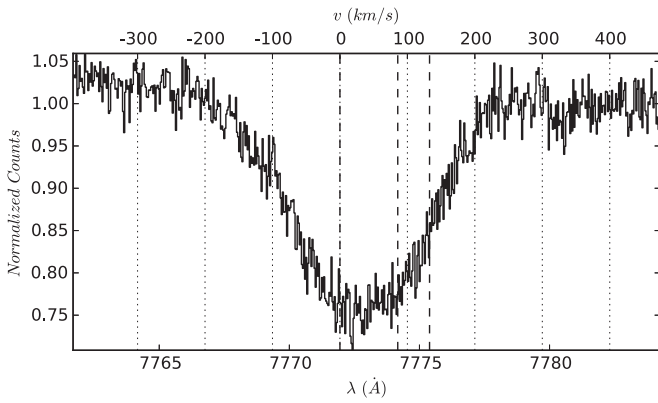
Figure 23. Blended O I λ7773 triplet absorption line profile of V899 Mon observed on 2014 December 22 using SALT-HRS. The vertical dashed lines mark the central positions of its triplet components at 7771.94, 7774.17, and 7775.39 Å.
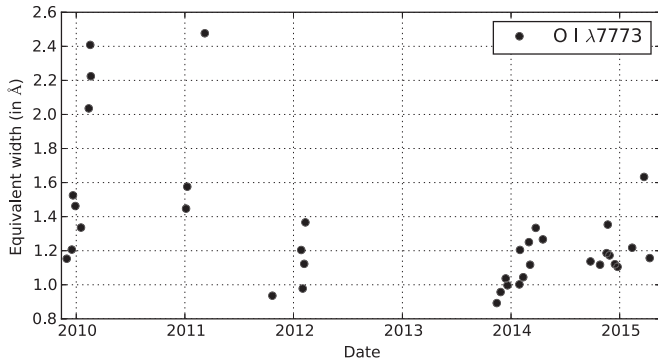
Figure 24. Evolution of equivalent width of O I λ7773 triplet, which traces the strength of turbulence in the disk of V899 Mon.

V899 Mon, increased suddenly during this short duration before the quiescence. In the final optical spectrum taken before the source transitioned from its first outburst phase to quiescent phase, we detect a sudden increase in equivalent width of the O I λ7773 absorption line (an indicator of turbulence). They are indicative of a highly turbulent activity around the V899 Mon source just before it transitioned to quiescent phase.

Accretion in low-mass YSOs is generally accepted to be via magnetospheric accretion funnels from disk to star. A large rate of accretion can provide a negative feedback in many ways. There are various semianalytic and numerical simulation studies in the literature on instabilities that can break and restart magnetospheric accretion (Kulkarni & Romanova 2008; Orlando et al. 2011; Blinova et al. 2015). For instance, the accretion can stop if the inner truncation radius of the disk moves outside the corotation radius (D'Angelo and Spruit 2010). In another scenario, the differential rotation between the inner accretion disk and the star can lead to inflation of the funnel, resulting in field lines opening and reconnecting, reducing accretion flow while enhancing outflow (Bouvier et al. 2003). These kinds of breaking mechanisms have the extra advantage that they can easily explain how a second outburst can restart without having to replenish the depleted disk within the short quiescence phase. Some other FUor sources like FU Ori, V1515 Cyg, and V2493 Cyg also show a short-duration dip in their light curves after they attained the initial peak of their outburst. All of them seem to

indicate a complex negative feedback loop in magnetospheric accretion.

It is interesting to note that both V899 Mon and V1647 Ori (discussed in Ninan et al. 2013) spent shorter duration in the first outburst compared to their ongoing second outbursts. The reason for the second outburst being more stable than the first outburst could be because of the change in the inner disk's physical parameters by the heating or the draining of the disk during the first outburst (such as the extent of the interaction region between magnetosphere and inner disk, their coupling, inner radius of the disk, etc.). In the case of V1647 Ori, from the stability in the phase of the X-ray accretion spot, Hamaguchi et al. (2012) had shown that the location of the spot of the accretion column shock on the star did not change significantly between the first and second outbursts. Hence, if the quiescent phase of V1647 Ori was due to disruption in magnetic funnel accretion, at least the base of the magnetic funnel on the star surface was not completely disrupted.

To summarize, even though we do not have direct observational evidence to support increased magnetic activity, the outflow and turbulence signatures in the spectrum and continuum flux are consistent with instability in the magnetic accretion funnel, and the timescales are strongly inconsistent with any other instability models that depend on critical disk surface densities to switch on and off the outburst.

4.2. V899 Mon: FUor or EXor

The empirical classification between FUors and EXors is based on the similarity in observed properties with classical FUors (FU Ori, V1515 Cyg, etc.) and EXors (EX Lup, V1118 Ori, etc.). Audard et al. (2014, p. 387) provide a detailed comparison of these objects from the literature. The $\sim$3 mag change in the brightness of V899 Mon during its outburst is typical of the EXors family of outbursts. On the other hand, the duration of outbursts in V899 Mon, $\sim$4 yr for the first outburst and greater than 3.5 yr for the ongoing second outburst, is significantly more than the typical duration EXors spend in outburst (less than 1–3 yr). Unlike V899 Mon, EXors also remain in quiescence longer than the time they spend in the outburst phase. However, V899 Mon's outburst timescales are still much less than classical FUors.

Spectroscopically, classical FUors have all optical and NIR hydrogen lines in absorption, while EXors have those lines in emission. In the case of V899 Mon, Hα and a small component of Hβ are in emission, while all the other hydrogen lines in optical and NIR are in absorption. CO bandheads starting at 2.29 μm are also in absorption. Hence, spectroscopically also V899 Mon lies between classical FUors and EXors. The $L_{\rm bol}$ estimates of V899 Mon from SED are greater than that of typical EXors, and they are less than that of classical FUors. The mass accretion rate during outburst phase is typical of EXors and is an order less than that of classical FUors.

Many of the recently discovered outbursts like V1647 Ori, OO Ser, etc., also show such intermediate properties between the classical bimodal classification of FUors and EXors. Discovery of more such intermediate-type outburst sources like V899 Mon indicates that this family of episodic accretion outbursts probably has a "continuum" distribution and not bimodal.

5. CONCLUSIONS

We have carried out a long-term monitoring of V899 Mon from 2009 September to 2015 April. During this period, V899 Mon underwent transition from the first outburst phase to the quiescent phase and then back to the second outburst phase. The following are the main results from our study.

1. Optical and NIR spectroscopy of V899 Mon confirms it to be a member of the FUors/EXors family of outbursts. Photometrically and spectroscopically V899 Mon's properties lie between EXors and classical FUors. But it is probably more similar to EXors than classical FUors.

2. At the end of 2010, V899 Mon abruptly ceased its first outburst phase and transitioned to the quiescent phase for a duration of little less than a year, immediately after which it returned to the second outburst.

3. Just before the break in the first outburst phase of V899 Mon, its spectra showed heavy outflow activity (indicated by a strong P Cygni) and increased turbulence.

4. The excess flux of the outburst initially had a cooler temperature than V899 Mon's photosphere and slowly became hotter as V899 Mon transitioned from the quiescent phase to the second outburst phase. This was seen in the change of $V - R$ and $V - I$ color of V899 Mon, which had reddest values during the intermediate transition period.

5. The outflows indicated by P Cygni profiles completely disappeared during the quiescent phase of V899 Mon and reappeared gradually only after V899 Mon reached its peak of the second outburst.

6. The high-resolution spectrum of the forbidden emission line profiles originating in outflows/jets shows blue-shifted velocity components extending up to $-500\,\mathrm{km\,s^{-1}}$, while the outflows traced by Hα P Cygni absorption profiles originating near the central star show complex multiple absorption components with velocities up to $-722\,\mathrm{km\,s^{-1}}$.

7. As expected from accretion outbursts, accretion rates estimated of V899 Mon from spectral lines show significant variation between first outburst, quiescent, and second outburst phases.

8. Since the A_V estimate from far-infrared is inconsistent with optical observations, V899 Mon is not embedded inside the far-infrared clump detected at its location. It is possible that our line of sight is through a cavity cleared out in the envelope. The clump is thermally influenced by the irradiation from V899 Mon since it showed variation in far-infrared flux between the first and the second outburst phases.

9. Since the disk replenishes slowly in the quiescent phase, all instability models that depend on the disk surface density to cross a certain threshold to trigger/stop an outburst are incompatible with V899 Mon's light curve. The case is similar to V1647 Ori.

10. The heavy outflow activity we detected just before V899 Mon transitioned to the quiescent phase is consistent with various magnetic instabilities that can arise in magneto-spheric accretion. Such instability-driven breaks in accretion can restart outburst immediately once the magnetic accretion funnel stabilizes.

REFERENCES

Ábrahám, P., Juhász, A., Dullemond, C. P., et al. 2009, Natur, 459, 224
Alcalá, J. M., Natta, A., Manara, C. F., et al. 2014, A&A, 561, A2
André, P., Men'shchikov, A., Bontemps, S., et al. 2010, A&A, 518, L102
Astropy Collaboration, Robitaille, T. P., Tollerud, E. J., et al. 2013, A&A, 558, 33
Audard, M., Ábrahám, P., Dunham, M. M., et al. 2014, Protostars and Planets VI, ed. H. Beuther, R. S. Klessen, C. P. Dullemond, & T. Henning (Tucson, AZ: Univ. Arizona Press), 387
Baraffe, I., Vorobyov, E., & Chabrier, G. 2012, ApJ, 756, 118
Bell, K. R., & Lin, D. N. C. 1994, ApJ, 427, 987
Bessell, M. S., & Brett, J. M. 1988, PASP, 100, 1134
Blinova, A. A., Romanova, M. M., & Lovelace, R. V. E. 2015, arXiv:1501.01948
Bouvier, J., Grankin, K. N., Alencar, S. H. P., et al. 2003, A&A, 409, 169
Bramall, D. G., Sharples, R., Tyas, L., et al. 2010, Proc. SPIE, 7735, 77354
Cardelli, J. A., Clayton, G. C., & Mathis, J. S. 1989, ApJ, 345, 245
Ciardi, D. R., Woodward, C. E., Clemens, D. P., Harker, D. E., & Rudy, R. J. 1998, AJ, 116, 349
D'Angelo, C. R., & Spruit, H. C. 2010, MNRAS, 406, 1208
Evans, N. J., II, Dunham, M. M., Jørgensen, J. K., et al. 2009, ApJS, 181, 321
Greene, T. P., Wilking, B. A., Andre, P., Young, E. T., & Lada, C. J. 1994, ApJ, 434, 614
Gullbring, E., Hartmann, L., Briceño, C., & Calvet, N. 1998, ApJ, 492, 323
Hamaguchi, K., Grosso, N., Kastner, J. H., et al. 2012, ApJ, 754, 32
Hamann, F. 1994, ApJS, 93, 485
Hamann, F., & Persson, S. E. 1992, ApJS, 82, 247
Hartigan, P., Edwards, S., & Ghandour, L. 1995, ApJ, 452, 736
Hartmann, L. 1998, Accretion Processes in Star Formation (Cambridge: Cambridge Univ. Press) 1998apsf.book.....H
Hartmann, L., & Kenyon, S. J. 1996, ARA&A, 34, 207
Herbig, G. H. 1977, ApJ, 217, 693
Hunt, L. K., Mannucci, F., Testi, L., et al. 1998, AJ, 115, 2594
Hunter, J. D. 2007, CSE, 9, 90
Ioannidis, G., & Froebrich, D. 2012, MNRAS, 425, 1380

Jones, E., Oliphant, T., Peterson, P., et al. 2001, SciPy: Open Source Scientific Tools for Python, [Online; accessed 2015-03-03]

Kenyon, S. J., Hartmann, L. W., Strom, K. M., & Strom, S. E. 1990, AJ, 99, 869

Kóspál, A., Ábrahám, P., Acosta-Pulido, J. A., et al. 2013, A&A, 551, A62

Kóspál, A., Ábrahám, P., Goto, M., et al. 2011, ApJ, 736, 72

Kulkarni, A. K., & Romanova, M. M. 2008, MNRAS, 386, 673

Landolt, A. U. 1992, AJ, 104, 340

Lombardi, M., Alves, J., & Lada, C. J. 2011, A&A, 535, A16

McGehee, P., Smith, J., Henden, A., et al. 2004, ApJ, 616, 1058

Men'shchikov, A., André, P., Didelon, P., et al. 2012, A&A, 542, A81

Meyer, M. R., Calvet, N., & Hillenbrand, L. A. 1997, AJ, 114, 288

Moran, J. M. 1983, RMxAA, 7, 95

Muzerolle, J., Hartmann, L., & Calvet, N. 1998, AJ, 116, 455

Naik, M. B., Ojha, D. K., Ghosh, S. K., et al. 2012, BASI, 40, 531

Ninan, J. P., Ojha, D. K., Bhatt, B. C., et al. 2013, ApJ, 778, 116

Ninan, J. P., Ojha, D. K., Ghosh, S. K., et al. 2014, JAI, 3, 1450006

Nisini, B., Milillo, A., Saraceno, P., & Vitali, F. 1995, A&A, 302, 169

Ojha, D. K., Ghosh, S. K., D'Costa, S. L. A., et al. 2012, in Astronomical Society of India Conf. Ser. 4, 191

Orlando, S., Reale, F., Peres, G., & Mignone, A. 2011, MNRAS, 415, 3380

Osterbrock, D. E., & Ferland, G. J. 2006, Astrophysics of Gaseous Nebulae and Active Galactic Nuclei (Mill Valley, CA: Univ. Science Books)

Rieke, G. H., & Lebofsky, M. J. 1985, ApJ, 288, 618

Robitaille, T. P., Whitney, B. A., Indebetouw, R., & Wood, K. 2007, ApJS, 169, 328

Safron, E. J., Fischer, W. J., Megeath, S. T., et al. 2015, ApJL, 800, L5

Scholz, A., Froebrich, D., & Wood, K. 2013, MNRAS, 430, 2910

Semkov, E. H., Peneva, S. P., Munari, U., et al. 2013, A&A, 556, A60

Siess, L., Dufour, E., & Forestini, M. 2000, A&A, 358, 593

Stahler, S. W., & Palla, F. 2005, The Formation of Stars (New York: Wiley, VCH)

Swarup, G., Ananthakrishnan, S., Kapahi, V. K., et al. 1991, CSci, 60, 95

van der Walt, S., Colbert, S. C., & Varoquaux, G. 2011, CSE, 13, 22

van der Walt, S., Schönberger, J. L., Nunez-Iglesias, J., et al. 2014, PeerJ, 2, e453

Wils, P., Greaves, J., Drake, A. J., & Catelan, M. 2009, CBET, 2033, 1

Wright, E. L., Eisenhardt, P. R. M., Mainzer, A. K., et al. 2010, AJ, 140, 1868

Zhu, Z., Hartmann, L., Gammie, C., & McKinney, J. C. 2009, ApJ, 701, 620